Ionics
https://doi.org/10.1007/s11581-026-07184-w

RESEARCH

DMSO-assisted copolymerization of acetone and sulfur and its application as a Li–S battery cathode

Ali Can Zaman[1] · **Figen Kaya**[1] · **Cengiz Kaya**[1]

Received: 2 March 2026 / Revised: 26 April 2026 / Accepted: 9 May 2026
© The Author(s), under exclusive licence to Springer-Verlag GmbH Germany, part of Springer Nature 2026

Abstract

There is an ongoing pursuit of new chemistries to advance lithium–sulfur (Li–S) battery technologies. Among these, electroactive sulfur-containing polymers have attracted significant interest. Here, we report a simple and novel synthesis route for producing a sulfur-rich polymer, acetone polysulfide (AcPS), using acetone, elemental sulfur, and dimethyl sulfoxide (DMSO) as starting materials. The reaction is performed in sealed vials at a moderate temperature of 130 °C, yielding organosulfur polymers containing carbonyl groups, condensation-derived conjugated carbon structures, and sulfur bridges between organic segments, with polymerized sulfur contents as high as ~59 wt%. Structural analyses confirm the formation of amorphous sulfur–carbonyl polymer networks without detectable crystalline sulfur domains. Electrochemical evaluation demonstrates that AcPS is active as a Li–S cathode material. In an optimized configuration employing a conductive carbon-coated separator, slurry-coated AcPS cathodes deliver a sulfur-specific discharge capacity of ~615 mAh g^{-1} at 0.2 C. Coulombic efficiency remains modest, stabilizing at approximately 90%, which is attributed to the dissolution of electroactive polymer-derived fragments and their transient interfacial accumulation on the Li anode, as supported by shuttle-current analysis and GITT-EIS. DOL/DME extraction further supports this interpretation, as removal of some soluble sulfur-containing polymer fractions suppresses the pronounced charge/discharge imbalance, causing the Coulombic efficiency to approach unity. Beyond materials development, this work also introduces a practical diagnostic rationale to distinguish conventional polysulfide shuttling from the migration of soluble polymer-derived redox-active species in Li–S cells.

Keywords Lithium–sulfur batteries · Sulfur–carbonyl polymers · Inverse vulcanization · Solvent-assisted polymerization · Electrochemical energy storage

Introduction

Sulfur possesses a high theoretical gravimetric capacity (1675 mAh g^{-1}) and a correspondingly high theoretical energy density at the active-material level when paired with a lithium anode (≈ 2600 Wh kg^{-1}) [1]. However, it is not easy to reach and retain this capacity. Because of several multiple challenges. Conventional sulfur cathodes are prepared by mixing sulfur, conductive carbon black and Polyvinyldene fluoride (PVDF). For these cathodes, severe capacity fade which can reach a loss between 60 and 85% isobserved within just 50 cycles [2, 3]. One reason behind is the shuttle effect. Generally ether based solvents are used in Li-S batteries since more common carbonate-based electrolytes react with polysulfides to form sulfide carbonate complexes [4]. However, polysulfide reaction byproducts, are generally soluble in organic ether based liquid electrolytes [5]. These intermediate polysulfides can migrate to the anode, where they irreversibly deposit after reduction forming insoluble Li_2S on the anode [6]. The shuttling results in low coulombic efficiency.

The reviewed interest to Li–S batteries was catalyzed by the study of Linda Nazar where she showed the physically confinement of sulfur in the cathode by embedding it in porous carbons [7]. Consistent with this strategy, mesoporous carbon–sulfur composites have been widely explored [8]. Nevertheless, physical confinement alone is

✉ Ali Can Zaman
aczaman@yildiz.edu.tr

[1] Department of Metallurgical and Materials Engineering, Yildiz Technical University, Davutpasa Campus, Esenler, Istanbul 34220, Turkey

Published online: 03 June 2026

often insufficient over extended cycling; sulfur can gradually redistribute and/or precipitate outside the carbon framework, allowing polysulfide shuttling to re-emerge. Heteroatom doped carbons (sulfur, nitrogen and oxygen) function better at preventing shuttling [5, 9, 10] as a result of intermolecular attractions between polysulfides and hosts [9]. In addition to carbons, polar additives/hosts can be used to confine polysulfides. Polar adsorbents have an ability to bind to polysulfides [11]. These polar substances can act as a catalyst or adsorbents and mitigate the shuttle effect [12]. Polymers [6], metal oxides [13, 14], metal sulfides [15], metal borides [16] can be used. Core-shell polar structures may also help to trap sulfur both with physical and chemical confinement, S S@PVP [17] and sulfur quantum dots@PVK [18] are notable examples. Functional interlayers could also mitigate the shuttle effect [19, 20]. But, altering the chemistry of the cathode is the most well-known choice to change the drawbacks of Li–S batteries [21]. In practice, effective suppression of shuttle reactions and improvement of sulfur utilization will likely require a combination of complementary strategies, such as conductive/functional separator coatings, optimized cathode architectures, gel or confined cathode designs, and tandem approaches involving catalytic or redox-mediator-assisted sulfur conversion [22].

Organosulfur compounds are promising materials in lithium-ion battery research [23]. Since the inception of utilization of tetraethylthiuram disulfide (TETD) in Li–S battery research, there has been many research acitivities about the subject [23, 24]. The general concept is to use covalent attachment of sulfur to anchor sulfur species [25, 26]. Although the formation of Li_2S during discharge is unavoidable, regulating its nucleation and growth is critical to maintain reversibility. By constraining sulfur species through covalent interactions, the accumulation of dense, passivating Li_2S deposits can be retarded, leading to more stable cycling behavior.

While the organic moieties decrease the specific capacity of the molecules, functional groups or organic sections have the advantage that they can facilitate polysulfide redox reactions, electrolyte wettability, cycling stability and capacity utilization as in the case of polar hosts. Polar functionalities such as CH_3O groups increase electrolyte wettability and capacity utilization [23, 27]. Shadike et al. produced 2,3,4,6,8,9,10,12-Octathia biscyclopenta [b, c]-5,11-anthraquinone-1,7-dithione (TPQD) carbonyl organosulfur compound by multi step route [28]. In their study, they have benefited from the presence of carbonyl and disulfide redox processes. However, they also admit that the redox processes due to disulfide bond causes kinetic issues during redox reactions. Chen et al. used 2, 5-dichloro-1, 4-benzoquinone as an electrolyte additive which covalently anchors generated polysulfides via nucleophilic substitution reactions [25]. Overall, linear chains of sulfur and carbonyl groups can be combined to make macromolecules that exhibit less shuttle and provide electrolyte wettability [23].

Another important perspective is cost and environmental friendliness. Choosing commercially available and inexpensive precursors makes the resulting products more viable for large-scale production. In addition, the production methods themselves play a critical role; they should be energy-efficient, scalable, and environmentally benign to ensure sustainable manufacturing.

Sulfur polymers emerge as a solution since it is possible to tune the chemical and physical properties of sulfur polymers by changing reaction conditions. The first reaction path is polysufide-ene type polymerization. In this polymerization, it is essential for the reaction to take place in an inert atmosphere [29]. Condensation polymerization is another approach. When chlorine/fluorine containing compounds are reacted with sulfur-containing inorganic compounds such as sodium sulfide in polar solvents, sulfur polymers can be obtained [30, 31]. This reaction also requires inert atmospheres to proceed and toxic solvents such as toluene/CS_2 or NMP are commonly used [32, 33]. Inverse vulcanization, a type of free radical polymerization, has been widely used for the production of sulfur polymers following the pinoeering work of Pyun et al. [34]. This method does not require inert atmosphere or chlorinated compounds. It is a bulk polymerization method which relies on reaction of sulfur radicals. With this method many compounds are formed which are used in Li–S research [35, 36]. The main limitation of this method is that it is generally restricted to the use of hydrophobic comonomers such as norbornene or divinyl benzene. However, a recent finding by Pyun et al. has shown that polymerization can also occur with comonomers previously thought to be incompatible with sulfur. This was made possible through the use of nucleophilic activators during polymerization experiments [37]. The activators or catalysts can be toxic, which does poses a risk.

Sulfur is hydrophobic and does not easily mix with polar compounds and it requires high temperatures to transform octasulfur into sulfur diradicals. However, this complicates use of low boiling point materials [38]. For example, Wwhen metacrylic acid was reacted with elemental sulfur, there is an incomplete reaction [39]. In addition, it seems that materials with already existing carbon-carbon double bonds are required in inverse vulcanization.

Krein et al. studied the reaction of polysulfide anions with α,β-unsaturated hydrocarbons in 1993 [40]. As a result of their work, they obtained polymeric by-products in certain cases. It is also known that conjugated carbonyl groups

are particularly important as they increase reaction kinetics and rate performance [23].

It is known that ketones that contain α-hydrogens can transform into unsaturated carbonyl compounds. Thus, under proper conditions without seeking unsaturated carbonyl compounds it may be possible to react ketones (simple carbonyl compounds) with elemental sulfur and the reaction product can be used as a cathode active material in Li–S batteries due to presence of polymerized sulfur.

Here we show that, DMSO is used to activate elemental sulfur and acetone (the simplest ketone) under mild synthesis conditions (130 °C) in a sealed vial to produce carbonyl/organosulfur polymers which contain up to 59 wt% polymerized sulfur. The influence of elemental sulfur loading in the reaction mixture was investigated to determine the maximum sulfur content that could be incorporated into the polymer structure. Excess elemental α-sulfur in some reaction products could be transformed into γ-sulfur with only 2 h of curing at 130 °C. The polymer material was successfully used as a Li–S battery cathode with the aid of a carbon separator coating and MWCNT addition. The current study provides valuable insights into the synthesis of acetone-derived sulfur polymers via dispersion polymerization using a DMSO–acetone–sulfur system, representing a solvent-assisted approach to inverse vulcanization.

Methods

Materials

Acetone (analytical grade)and dimethyl sulfoxide (DMSO, anhydrous, ≥99.9%) were purchased from Merck. Elemental sulfur (powdered, ≥99.5%) was purchased from Thermo Fisher. All reagents were used without further purification. All reactions were conducted under ambient atmospheric conditions. Multi walled carbon nanotubes (MWCNTs) were obtained from Thomas Swann Co. (30 nm diameter, 30 µm length). N-methyl-2-pyrrolidone (NMP) was purchased from Merck.

Polymer synthesis procedure

Series of acetone-derived sulfur polymers were synthesized via a one-pot solvothermal reaction using sealed vials. In a typical procedure, 0.125 g of elemental sulfur (equivalent to 3.9 mmol) was placed in a 20 mL crimp-sealed glass vial equipped with a PTFE-lined crimp cap. Depending on the desired feed ratio, acetone and DMSO were added in molar ratios relative to sulfur as follows: 4:1:25, 2:1:25, 1:1:25, or 0.5:1:25 (acetone : sulfur : DMSO, molar basis). These feed ratios were selected to investigate the effect of acetone concentration on the extent of polymerization and determine the maximum amount of sulfur that could be successfully embedded into the polymer network. All vials contained 0.125 g sulfur, and the quantities of acetone and DMSO were scaled accordingly based on sulfur's molar amount (3.9 mmol). Once the reactants were loaded, the vial was sealed securely with the PTFE-lined cap, ensuring an airtight environment. The sealed vial was then immersed in a preheated oil bath at 130 °C and maintained for 24 h to allow reaction.

After the reaction, the vials were allowed to cool to room temperature before opening. The resulting viscous or semi-solid reaction mixture was diluted and stirred thoroughly in a large excess of deionized water, during which gas bubble formation was observed—likely due to hydrolysis or release of residual volatile by-products. The mixture was then subjected to vacuum filtration and washed extensively with deionized water to remove unreacted reagents and soluble by-products. Following water washing, the material was further rinsed with 25–50 mL of isopropyl alcohol (IPA) to aid in the removal of by-products. The filtered material was dried in an oven at 100 °C overnight (∼12–16 h). The resulting dried material was then ground in a mortar to obtain a homogeneous powder. At this stage, the materials were considered "uncured." The ground powders were subjected to thermal curing at 130 °C for 2 h in air to enhance crosslinking. The final materials were labeled based on their acetone-to-sulfur molar ratios as: 4AcPS, 2AcPS, 1AcPS, 0.5AcPS. Table 1 shows the properties of the obtained products. The table lists product yield before and after curing, elemental

Table 1 Summary of acetone polysulfide (AcPS) samples synthesized at different acetone/sulfur/DMSO molar ratios

Material	Acetone/S/DMSO molar ratios	Product weight after synthesis	Prepolymer yield (%)	Yield after curing based on prepolymer (%)	Elemental sulfur phase (before → after cure)	Sulfur quantity (wt%) (EDS)	Review
4AcPS	4/1/25	0.16	15.51	98.4	No	53.95	Black color & easy to filter
2AcPS	2/1/25	0.151	26.1	98.4	No	59.26	Black color & relatively easy to filter
1AcPS	1/1/25	0.128	36	97.5	α-Sulfur/γ-monoclinic sulfur	65.47	Black color & very hard to filter
0.5AcPS	40.51/25	0.1136	48	94.7	α-Sulfur /γ-monoclinic sulfur	73.48	Brown & very hard to filter

sulfur content, sulfur quantity determined by EDS, and qualitative observations of color and filterability.

Electrode preparation, separator coating procedure and cell assembly

For electrochemical testing, 0.5 g of cured 2AcPS was placed in an 80 mL stainless steel ball milling jar along with 15 stainless steel balls (each 5 mm in diameter). The 2AcPS was mixed with Super P conductive carbon and multi-walled carbon nanotubes (MWCNTs) in a dry state using a planetary ball mill (Fritsch, Pulverizette 6) at 600 rpm for 15 min. The mass ratio of components was maintained as 70:15:5:10 for 2AcPS: Super P: MWCNTs: PVDF.

After dry milling, a PVDF solution in N-methyl-2-pyrrolidone (NMP) was added, and wet milling was performed under the same speed using 12 milling cycles, each consisting of 10 min milling followed by 1-minute rest. The coated electrodes were initially dried at 80 °C for 12–16 h to remove residual solvent. Following drying, the electrodes were heat-treated at 130 °C for 2 h to promote adhesion and initiate partial curing of the polymer binder. 2AcPS served as the sulfur-containing cathode material, while the electrochemically active mass used for capacity calculations was taken as the sulfur present in electroactive S–S bonds. Circular cathode discs (1 cm diameter) were then punched out, with typical active material loadings ranging from 1 to 1.3 mg cm^{-2}. The loading of active material (sulfur present in electroactive S–S bonds) was around 1.82 mg per electrode. Accordingly, the sulfur loading values and the electrolyte-to-sulfur (E/S) ratio reported in this work were calculated using this electroactive sulfur content. The electrolyte used in all cells was 1 M LiTFSI dissolved in a 1:1 (v/v) mixture of 1,2-dimethoxyethane (DME) and 1,3-dioxolane (DOL), with 1 wt% $LiNO_3$ as an additive to stabilize the lithium metal anode. The electrolyte-to-sulfur (E/S) ratio was set at 20 µL mg^{-1} based on sulfur content. The separator membrane was soaked in electrolyte prior to assembly.

1.7–2.0 mg per electrode attempts to fabricate cathodes with higher areal loadings (e.g., ~2 mg cm^{-2}) were unsuccessful, as the films tended to delaminate and peel off from the aluminum current collector during or after drying. Therefore, all electrochemical tests in this study were performed using electrodes with moderate areal loading to ensure structural stability and reliable performance.

To mitigate the shuttling of dissolved polymer-derived sulfur species, separator coatings were prepared using a Super P–PVDF composite similar to the method reported by Yao et al. [1] and Chung et al. [41]. A 9:1 mass ratio of Super P to PVDF was dispersed in NMP and mixed via ball milling under similar conditions to electrode slurry preparation. The slurry was then coated onto Celgard 2400 polypropylene membranes using the doctor blade method. These membranes were dried at 60 °C and subsequently punched into 19 mm diameter circular separators for coin cell use. Areal loading of Super P is between 0.20 and 0.225 mg cm^2. The cells containing Super P coated separator are denoted as CS-2AcPS.

All coin-type (CR2032) half cells were assembled in an argon-filled glove box (Mbraun Unilab) with O_2 and H_2O levels below 0.1 ppm. The 2AcPS cathode served as the working electrode, lithium metal foil as the counter/reference electrode.

To examine the effect of DOL/DME soaking, the polymer was dispersed in a DOL/DME mixture at a concentration of 25 g L^{-1} and kept for 24 h. After soaking, the mixture was filtered, and the insoluble residue was collected for further analysis. The recovered residue showed an approximately 7% decrease in mass compared with the initial polymer. Cathodes were then prepared from this residue using the same procedure described for the unsoaked polymer cathodes. Electrochemical tests were carried out under identical conditions, and a carbon-coated separator was also used in these measurements. Cyclic voltammetry (CV) and galvanostatic charge–discharge tests were performed to evaluate the electrochemical behavior of the residue. In addition, the supernatant obtained after soaking was analyzed by UV–Vis spectroscopy.

Electrochemical tests

All electrochemical measurements were carried out using a Biologic SP-150e potentiostat/galvanostat. The experiments were conducted at room temperature (~25 °C). Cyclic voltammetry (CV) and galvanostatic charge–discharge tests were performed within a voltage window of 1.6–2.8 V vs. Li/Li^+. The cells were first allowed to rest at open-circuit voltage (OCV) for 18 h after assembly to ensure electrode–electrolyte equilibration. Prior to performance evaluation, cells were preconditioned at 0.05 C for two full cycles to stabilize the electrode interfaces and activate the sulfur-containing cathode material. Charge discharge tests were conducted between 2.8 V and 1.75 V due to irreversible reduction of $LiNO_3$ at low voltages [42]. The capacity and current rates were calculated based on the weight of the active sulfur content.

To evaluate the internal and electrolyte resistances during cycling, a combination of the galvanostatic intermittent titration technique (GITT) and electrochemical impedance spectroscopy (EIS) was employed. The internal resistance change during charge-discharge processes can be quantified by using GITT method:

$$\triangle R_{internal}\ (\Omega) = \frac{|\triangle V_{QOCV-CCV}|}{I_{applied}}$$

ΔV is the difference between quasi open circuit voltage and closed-circuit voltage. I is the applied current during charge or discharge. At each GITT step, impedance measurements were also conducted to calculate electrolyte resistance which is revealed by high frequency intercept values of each impedance spectra.

Additionally, at each GITT step, immediately following the galvanostatic pulse and before applying the next current, impedance measurements were performed to determine the electrolyte resistance. The electrolyte resistance was obtained from the high-frequency intercept of each Nyquist plot with the real axis (Z'). These measurements were repeated at various depths of discharge (DoD) to assess the evolution of both internal and electrolyte resistances as a function of electrochemical progression.

Material characterization

Solid-state ^{13}C nuclear magnetic resonance (NMR) spectra were acquired on a Bruker Avance Neo 500 spectrometer using the cross-polarization/magic-angle spinning (CP/MAS) technique, with a contact time of 2 ms and a spinning speed of 12 kHz. Powder X-ray diffraction (XRD) patterns were obtained using a PANalytical X'Pert PRO diffractometer equipped with Cu Kα radiation (λ = 1.5406 Å) to analyze the crystalline structure of the samples. Differential scanning calorimetry (DSC) was performed using a Netzsch, DSC 3500 Sirius instrument under a nitrogen atmosphere at a heating rate of 10 °C min^{-1}. In each analysis, the sample was first heated to 130 °C to simulate the curing/preconditioning process, then cooled to −60 °C, followed by a second heating cycle. Only the second heating curve was used for thermal interpretation to eliminate thermal history effects. Thermal decomposition behavior was further studied using simultaneous differential thermal analysis and thermogravimetric analysis (DTA–TG) with a Seiko Instruments SII, Exstar 6300 TG/DTA instrument under nitrogen flow. Fourier-transform infrared (FTIR) spectra were recorded using a PerkinElmer Spectrum 100 spectrometer to identify functional groups present in the polymer structures. In addition, the gaseous products evolved during thermal decomposition were analyzed by TG–FTIR to gain further insight into the decomposition behavior and structural features of the polymers.

Scanning electron microscopy (SEM) and scanning transmission electron microscopy in SEM (STEM-in-SEM) were carried out using a Thermo Scientific Apreo 2 S LoVac microscope to examine electrode material morphology and elemental distribution. Energy-dispersive X-ray spectroscopy (EDS) analysis was performed at multiple regions under low vacuum conditions (~10 Pa) to prevent charging and accommodate non-conductive surfaces. Raman spectroscopy analyses were conducted using an Edinburgh Instruments RM5 Raman microscope equipped with a 532 nm excitation laser, to analyze the vibrational characteristics of sulfur and carbon-containing species. X-ray photoelectron spectroscopy (XPS) measurements were performed with a Thermo Scientific K-Alpha spectrometer (aluminum K-Alpha radiation) to investigate surface chemical composition and oxidation states. UV-Vis absorption spectroscopy measurements were conducted in Shimadzu UV-2600 UV-Vis Spectrophotometer using sealed quartz cuvettes (Starna cells).

Results

Vulcanization is a free radical polymerization with ionic and radical pathways which may present concurrently [43]. So along with radicals (•S_n•), ionic sulfur species (Sn^{2-}, $S_n^{\bullet-}$) may form after the reaction with organic molecules. Anions can abstract hydrogen at the alpha position relative to the double bonds in organic molecules [43, 44]. As a consequence reactive sites are generated on organic molecules. These reactive sites react with sulfur species to form a cross-linked structures. And, this mechanism can be extended to α,β-unsaturated carbonyl compounds [40]. We postulate that even a simple ketonic molecule such as acetone could be used as a starting material for that purpose. We note, acetone can undergo aldol condensation under acidic or basic conditions to form α,β-unsaturated carbonyl compounds [45]. By this way, acetone can in-situ transform into α,β-unsaturated carbonyl species in the reaction environment and undergo radical addition with sulfur species [46].

However, preliminary tests revealed that reaction of acetone and elemental sulfur do not appreciably proceed without an additive. Firstly, an activator solvent is needed to dissolve S_8 and promote its transformation into linear sulfur species at relatively low temperatures. Secondly, the activator solvent facilitates conversion of acetone into α,β-unsaturated intermediate compound, which take part in reaction with sulfur species.

Nucleophilic activation was found to be useful in inverse vulcanization [37]. For example, Tonkin et al. used pyridine as a repair agent and demonstrated that pyridine can promote ring opening reaction of S_8 [47]. Similar to those works, a nucleophilic solvent in polymerization reactions can be useful for its nucleophilic character and high boiling point. It should readily dissolve both acetone and S_8 [48].

It is postulated that DMSO facilitates mass transport and promotes the formation of sufficient amounts of sulfur diradicals at relatively low temperatures (T ≥ 130 °C). Operating at such temperatures also minimizes H_2S generation possibility, which otherwise could lead to pressure buildup and reduced product yield [43]. Furthermore, DMSO–lithium polysulfide solutions are known to exhibit a characteristic blue color, attributed to the radical-stabilizing ability of DMSO. This radical stabilization suggests an additional role for DMSO as a vulcanization accelerator: similar to conventional accelerators or activators, DMSO may positions radicals near the crosslinker and likely lowers the energy barrier for bond formation [49].

DMSO also provides suitable environment for the transformation of acetone into unsaturated compounds. DMSO does not directly convert acetone into an α,β-unsaturated compound (at least on its own), but it can facilitate this transformation when used in combination with sulfur, such as sulfur anions (results in heterolytic cleavage of S_8); sulfur anions or radicals may abstract α-hydrogens from acetone and promote subsequent condensation reactions. This can initiate aldol-type condensations. Overall, the possible formation reactions of acetone polysulfide through a free-radical mechanism are shown in Fig. 1. It should be noted that the final structure is presented only as a simplified representation of a possible sulfur-containing motif and does not account for the conjugated carbon environments revealed by the NMR analysis. All reactions occur in a single synthesis step (Fig. 1a). The steps are: (b) Homolytic and heterolytic cleavage of S_8, (c) Abstraction α-hydrogens from acetone and enolate formation, (d) Aldol condensation reactions to form α,β-unsaturated carbonyls, (e) cross-linking carbonyl compounds between sulfur radicals.

XRD analyses

XRD can detect unreacted sulfur. There is no difference between cured and as synthesized states of 2AcPS and 4AcPS and both are amorphous materials with only broad peaks around 25º (Fig. 2a). This suggests that sulfur present in these samples is in polymerized form, which will be corroborated via EDS. However, in the as-synthesized state 1AcPS and 0.5AcPS have unpolymerized α-sulfur (Fig. 2b). Interestingly, after curing, excess unpolymerized α-sulfur transforms into γ-sulfur. This is the first time in literature that this rare form of sulfur is easily obtained by curing excess sulfur in a sulfur polymer environment. γ-sulfur is important. In some studies, it was shown to be a good electroactive material in Li–S batteries since it can allow solid-state transformations [50].

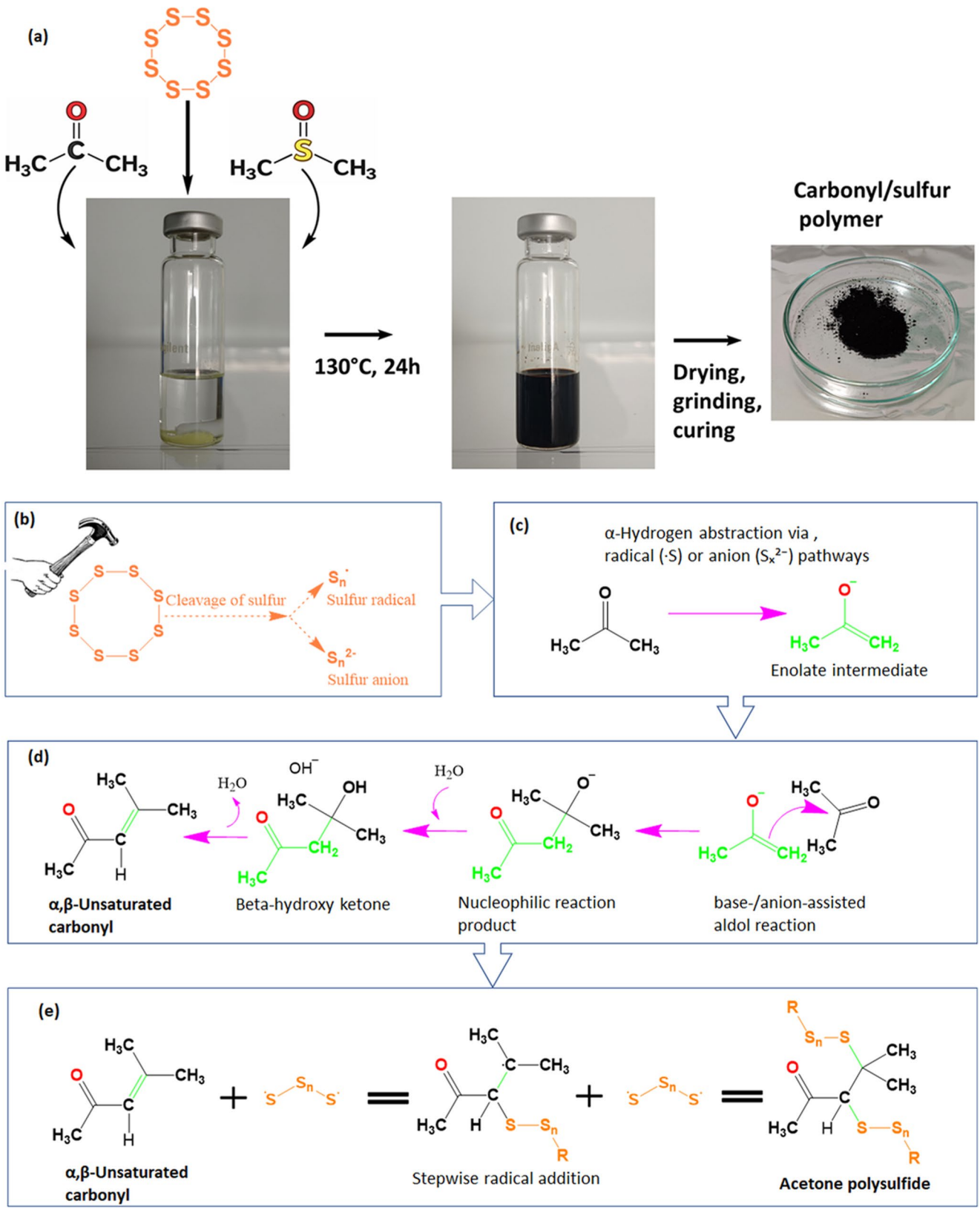
Fig. 1 (**a**) Synthesis procedure and proposed one-pot pathways for acetone–polysulfide network formation in an activator solvent: (**b**) Thermal/solvent-assisted homolytic and heterolytic cleavage of S_8 generating $S^{\bullet}/S_x^{\bullet}$ and S_x^{2-}. (**c**) α-Hydrogen removal from acetone via radical abstraction by sulfur species and/or deprotonation by polysulfide anions, yielding carbon-centered radical/enolate intermediates. (**d**) Aldol condensation provides α,β-unsaturated carbonyls. (**e**) Stepwise addition of sulfur radicals (or S_x^{2-}) across C = C followed by propagation/coupling to form C–S–S_n–C cross-links, giving acetone polysulfide. Note: The final AcPS structure does not show all structural features of the real material

Thermal analysis

The thermal behavior of the polymers was investigated using thermogravimetric analysis (TG) and differential scanning calorimetry (DSC) (Fig. 3a–d). Elemental sulfur undergoes complete evaporation at temperatures below 400 °C. In contrast, the synthesized AcPS samples exhibit at least two distinct weight-loss events and do not show complete mass loss even at elevated temperatures, indicating the formation of a thermally stable, cross-linked polymeric structure (Fig. 3a).

The DTG curves of 2AcPS and 4AcPS are nearly identical, suggesting similar molecular architectures and cross-linking characteristics (Fig. 3b). The first weight-loss event, occurring in the temperature range of 274–281 °C, is attributed to S–S bond cleavage and the release of polymerized sulfur species, consistent with previous reports [36]. A second weight-loss peak centered around 490 °C is observed and is likely associated with further degradation of the cross-linked polymer backbone through more complex decomposition pathways. The second mass-loss peak is almost absent in 0.5AcPS, which can be attributed to its higher content of unpolymerized elemental sulfur that volatilizes at lower temperatures. For 1AcPS and 0.5AcPS, both polymerized sulfur and elemental sulfur coexist in varying proportions, resulting in overlapping thermal decomposition behaviors.

The presence of two mass loss peaks complicates determination of sulfur content of polymers as the mass loss cannot be attributed solely to sulfur evaporation. It is possible to determine electroactive sulfur content in S-S bonds through isothermal heating [51]. The S-S bond is weaker than the C-S bond. The synthesized materials were held below second mass loss peak, but above the first mass loss peak, removing most of the polymerized sulfur (Fig. 3c). The remaining material quantity was used to calculate electroactive sulfur content assuming that sulfur bonded to carbon atoms do not actively participate in redox reactions [51]. In this way, it is revealed that ~ 45 wt% of both 4AcPS and 2AcPS is sulfur in S-S bonds. However, this estimation should be regarded as approximate rather than absolute. To further examine the decomposition behavior, TG-FTIR analysis was performed on 2AcPS (Fig. S1). The results indicated the evolution


(a)
130°C, 24h
Drying, grinding, curing
Carbonyl/sulfur polymer
(b)
Cleavage of sulfur
Sulfur radical
Sulfur anion
(c)
α-Hydrogen abstraction via , radical (·S) or anion (S_x^{2-}) pathways
Enolate intermediate
(d)
α,β-Unsaturated carbonyl
Beta-hydroxy ketone
Nucleophilic reaction product
base-/anion-assisted aldol reaction
(e)
α,β-Unsaturated carbonyl
Stepwise radical addition
Acetone polysulfide

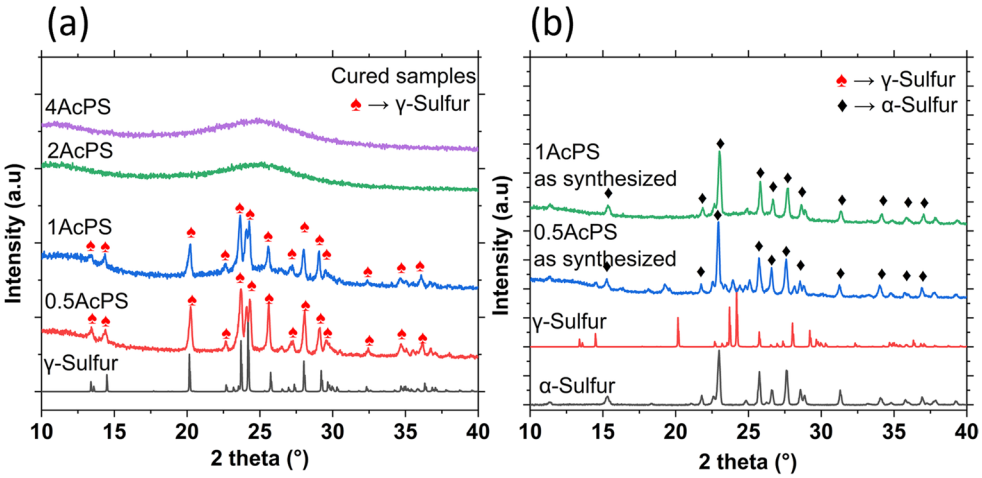


Fig. 2 (**a**) XRD patterns of cured samples that have varying Acetone/sulfur ratio in the reaction mixture. (**b**) XRD patterns of 1AcPS and 0.5AcPS in as-synthesized state (XRD patterns of cured or uncured 2AcPS and 4AcPS are almost identical)

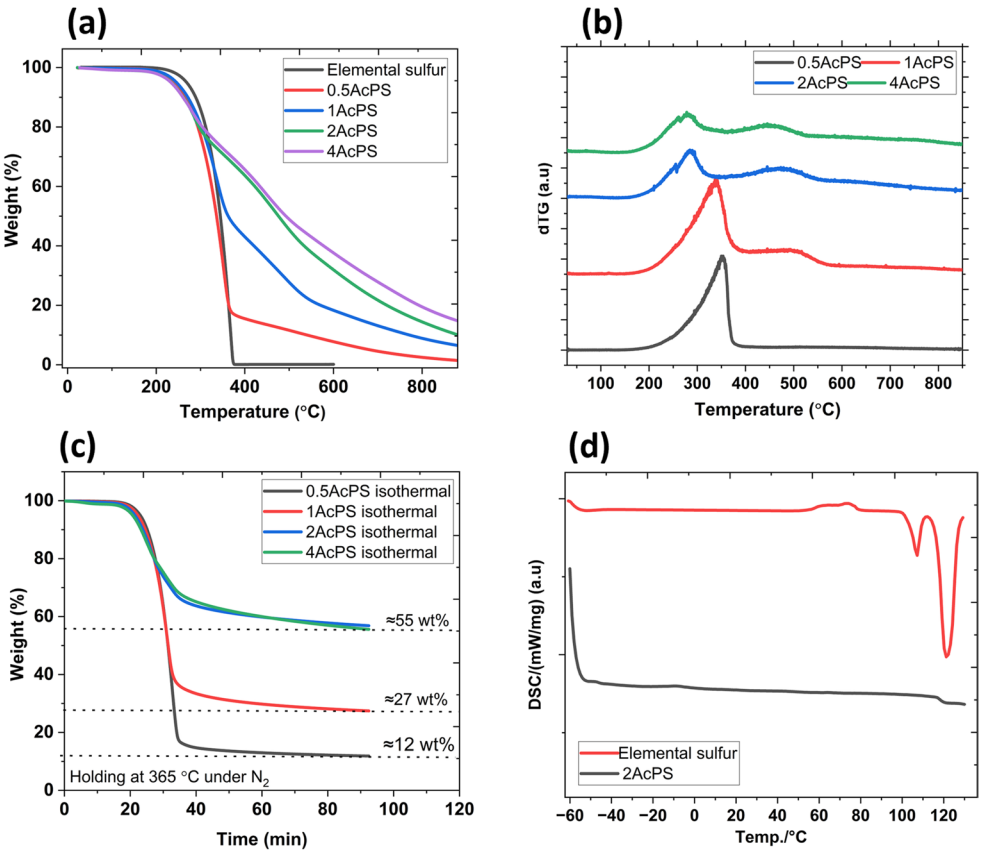


Fig. 3 (**a**) TGA of samples and elemental sulfur, (**b**) DTG of samples and elemental sulfur, (**c**) TGA of samples that are subjected to isothermal hold at 365 °C, (**d**) DSC of 2AcPS and elemental sulfur

of sulfur-containing as well as carbon-containing gaseous species, suggesting that the first mass-loss region may also involve decomposition of sulfur-containing organic motifs rather than the exclusive release of polymerized sulfur. Therefore, the calculated electroactive sulfur content should be considered an approximate estimate. The band at approximately 2049 cm^{-1} was assigned to carbonyl sulfide (COS/OCS). ~1535–1537 cm^{-1} peak suggests CS_2. ~2295–2385 cm^{-1} region can be attributed to CO_2.

2AcPS is further characterized by DSC (Fig. 3d). In DSC curve of elemental sulfur the transformation of α-S and β-S takes place at around 106 °C and the second endothermic peak is related to melting of sulfur [44]. Unlike elemental sulfur there is no detectable elemental sulfur in the structure in 2AcPS. The feature around 90 °C in 2AcPS is perhaps related to the glass transition temperature (Tg). Besides, only one Tg step may indicate one type of random copolymer [52]. There may be small quantities of undedectable sulfur.

Raman, infrared and X-ray photolectron spectroscopy analyses

Formation of a polymeric network free of elemental sulfur in 2AcPS and 4AcPS was further corroborated by Raman spectroscopy (Fig. 4a). Elemental sulfur has peaks at 157 cm^{-1}, 220 cm^{-1} 438 cm^{-1} and 475 cm^{-1}. The peaks at 157 and 220 cm^{-1} is indicative of elemental sulfur. Thus, 1AcPS and 0.5AcPS contain unpolymerized sulfur. But 2AcPS and 4AcPS only contain a broad peak at 464 cm^{-1}, which is related to S-S-S vibrations in polymerized linear sulfur Sects [53, 54]. FTIR analyses were performed to elucidate organic sections in the polymer (Fig. 4b-c). Compared to 1AcPS and 0.5AcPS, the 2AcPS and 4AcPS samples exhibit more distinct peaks in the spectra. This is likely because sulfur, which dominates the composition of 1AcPS and 0.5AcPS, cannot be effectively detected within the current spectral window. The peak at 1706 cm^{-1} indicates the presence of carbonyl (C = O) groups. The band at 1638 cm^{-1} may be tentatively assigned to conjugated C = O stretching and/or C = C stretching in an unsaturated framework, whereas the feature at 1605 cm^{-1} is consistent with C = C stretching vibrations. The broad band observed around 1203 cm^{-1} could be associated with either C–O bonds or S = O groups in the molecular structure. These spectral features suggest the presence of carbonyl groups both adjacent to and isolated from C = C bonds. The persistence of the C = C signal indicates that the reaction conditions did not completely consume all the double bonds, meaning that some crosslinker molecules remain unsaturated. Additionally, the presence of C–OH groups or other oxygen-containing functionalities, apart from carbonyls, is possible. This assumption is supported by the high solubility of 2AcPS in basic aqueous solutions (NaOH), which may be the result of sodium salt formation. It is known that acidic functional groups tend to react with bases resulting in the formation of corresponding salts [55]. This may indicate that a fraction of the oxygen atoms is present as hydroxyl (–OH) groups rather than in quinone or carbonyl functionalities. It is also possible that the peaks observed in the 1705 cm^{-1} and 1203 cm^{-1} regions are related to the presence of carboxylic acid (–COOH) groups. However, the broad O–H stretching band typically seen around 3200 cm^{-1} was not clearly detected in any of the samples, which limits conclusive assignment (Fig. 4c).

SEM analyses

SEM and STEM were performed to assess structural and compositional homogeneity of the cured polymer samples (Fig. 5). Backscattered electron (BSE) imaging was used to identify chemical inhomogeneities (Fig. 5a–d). Although the presence of elemental sulfur was expected, no distinct compositional contrast was observed in the 0.5AcPS and 1AcPS samples, indicating apparent chemical uniformity at the micron scale. Notably, 0.5AcPS exhibited pronounced macroporosity, while increasing the acetone content in the reaction mixture led to progressively denser morphologies. Both 2AcPS and 4AcPS formed compact, low-porosity structures, with 4AcPS displaying the densest morphology among the series (Fig. 5c-d). The absence of visible microporosity in these higher-acetone-ratio samples is attributed to increased crosslinking density within the polymer network, resulting in more tightly packed structures.

STEM-in-SEM analysis was further conducted on the 2AcPS sample to investigate nanoscale morphology and elemental distribution (Fig. 5e–g). This sample was selected for advanced characterization because it exhibited the highest fraction of polymerized sulfur while being free of residual elemental sulfur, and it was therefore chosen as the primary candidate for subsequent electrochemical studies. The bright-field (BF) image (Fig. 5e) shows a non-porous, compact internal structure. The dark-field (DF) image indicates a lack of embedded high-atomic-number inclusions such as crystalline sulfur domains (Fig. 5f). HAADF mode further supports the conclusion that sulfur is dispersed

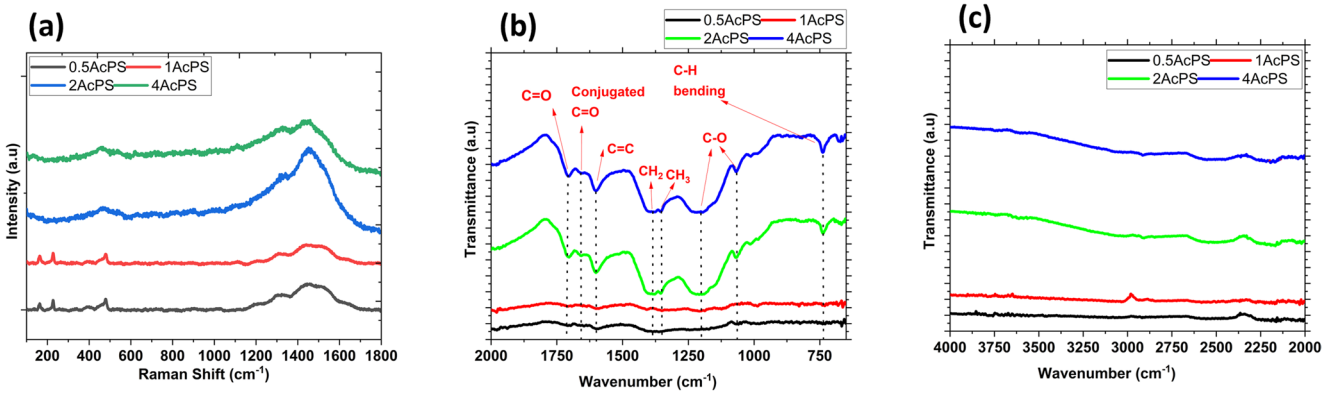


Fig. 4 (**a**) Typical Raman spectrum of the cured samples, (**b**) FTIR spectra of cured samples, (**c**) FTIR spectra of cured samples between 4000–2000 cm^{-1}

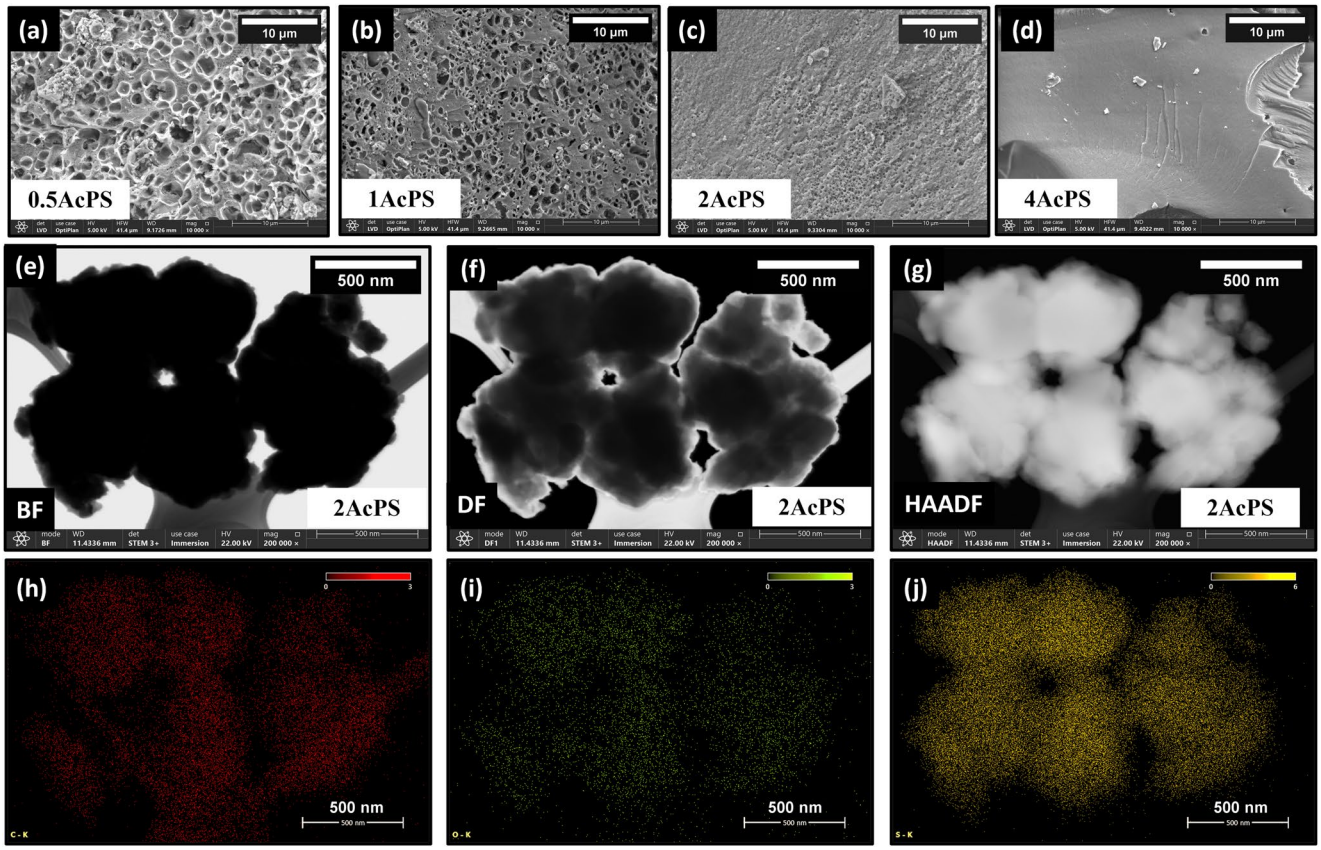


Fig. 5 SEM images of the cured polymer products at different acetone-to-sulfur ratios: (**a**) 0.5AcPS, (**b**) 1AcPS, (**c**) 2AcPS, and (**d**) 4AcPS. STEM-in-SEM analysis of the cured 2AcPS sample: (**e**) bright-field (BF) image, (**f**) dark-field (DF) image, and (**g**) high-angle annular dark field (HAADF) image. Elemental mapping of the same region showing the distribution of (**h**) carbon (C Kα), (**i**) oxygen (O Kα), and (**j**) sulfur (S Kα)

within the polymer network rather than being phase-separated (Fig. 5g).

XPS and NMR analyses

XPS was conducted to examine the surface chemistry of the 2AcPS sample (Fig. 6a-c). The C 1s spectrum was deconvoluted into three main peaks. Notably, no peak correction or binding energy calibration was applied (e.g., using adventitious carbon), so peak assignments are made relative to the observed positions. The peak at ~ 285 eV is attributed to C–C and C–S bonds, which are consistent with the organic polymer backbone and thioether crosslinks (C = C/C-C bonds generally appear at 284.5–285 eV [56, 57]). The strong feature at ~ 288 eV is indicative of carbonyl (C = O) functionalities [58], supporting the incorporation of ketone-derived structures in the polymer matrix. The broad signal near ~ 290 eV may partially result from surface oxidation. It could also reflect the presence of minor amounts of oxidized sulfur groups, such as C–SO_2– (sulfone) moieties, potentially formed by oxidation of thioether linkages or incorporation of DMSO. Deconvolution of the O 1s spectra reveals 2 contributions (Fig. 6b). The peak at 531 eV is due to C = O [59]. The other peak is at 533.0 eV, which can be attributed to C-O. The quantity of C-O is high, perhaps due to oxidation of the sample surface. Interpreting S 2p spectra in XPS for organosulfur compounds is challenging, particularly when trying to differentiate S-S and C-S bonds since there is close electronegativity of the corresponding atoms. Due to spin orbit coupling the S 2p spectra is split into S 2p$_{3/2}$ and S 2p$_{1/2}$. These components have an areal intensity ratio of 2:1 (S 2p$_{3/2}$ is more intense than S 2p$_{1/2}$). The energy separation is around 1.18 eV, which is dependent on the environment. Considering these constraints, the deconvolution of S 2p spectrum is shown in Fig. 6c. Unfortunately, very broad peaks are observed in the high binding energy region, which we could not eliminate. This may be the result of instrumental issues. But we can say that 3 different chemical environments present in the sample, C–S (164–165 eV, ~ 61%) [60], -S–S- (16–166 eV, ~ 25.5%) and SO_x (168 − 16 eV, ~ 12.2%) [61]. Oxidized sulfr may be the result of incorporation of DMSO to the polymer system. Since the XPS spectra exhibit features indicative of oxidized sulfur species, a control experiment was conducted in which elemental sulfur

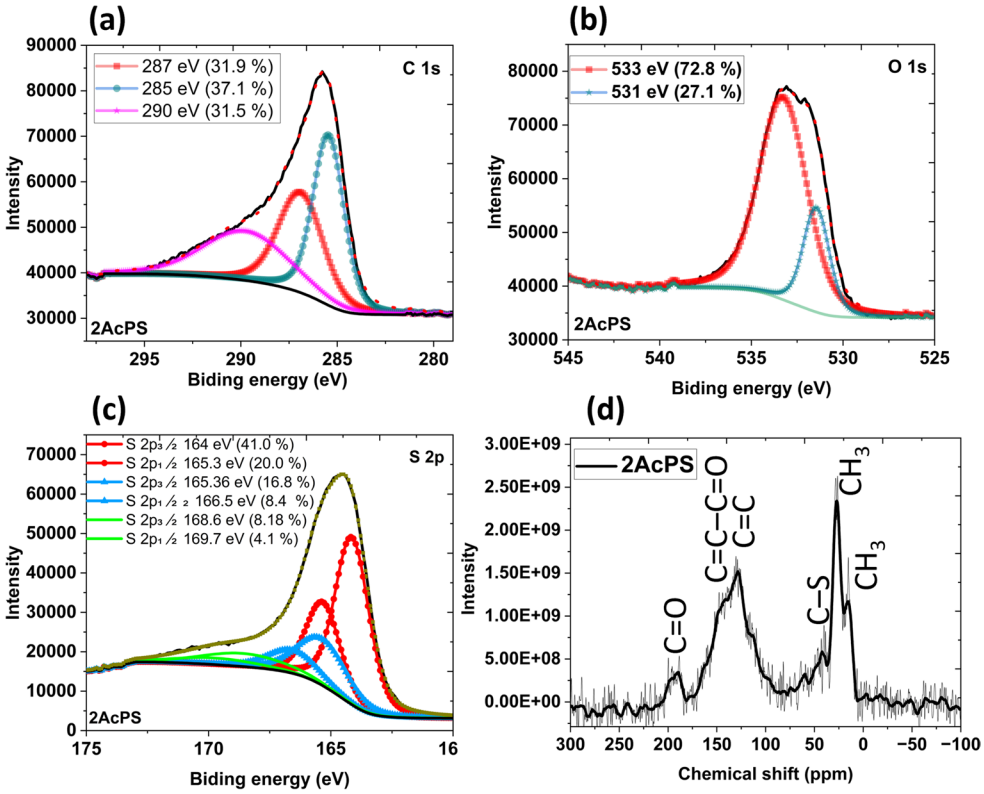


Fig. 6 High resolution XPS spectra: (**a**) C 1s, (**b**) O 1s and (**c**) S 2p and (**d**) is solid-state ^{13}C CP/MAS NMR spectrum of 2AcPS

was mixed with DMSO and subjected to the same synthesis conditions. Under these conditions, no polymeric material was formed. Instead, a yellow precipitate was observed in a transparent liquid phase. In contrast, when acetone, DMSO, and elemental sulfur were combined under identical conditions, polymerization occurred, yielding a solid polymeric product. This comparison suggests that DMSO alone does not induce polymer formation but may become activated in the presence of acetone and sulfur and partially participate in the resulting polymer structure.

The solid-state ^{13}C CP/MAS NMR spectrum of 2AcPS is shown in Fig. 6d. A resonance in the 188–200 ppm region is assigned to carbonyl carbons [31, 33, 43, 62] confirming the presence of ketone-type functionalities in the polymer. A broad resonance centered at approximately 130 ppm, with a downfield shoulder extending toward ~ 146–155 ppm, is attributed to unsaturated/conjugated sp^2 carbon environments [33]. The downfield shoulder may arise from more deshielded conjugated carbons, possibly including enol- or oxygen-substituted sp^2 carbons. These features support the formation of condensation-derived conjugated structures, consistent with the in-situ transformation of acetone into unsaturated intermediates prior to reaction with sulfur radicals. No distinct resonance attributable to abundant C–O–C-type ether carbons is observed in the expected > 50 ppm region [62]. The resonance at 39 ppm is assigned to aliphatic carbons bonded to sulfur and/or located alpha to carbonyl groups [43, 62]. The resonance at ~ 39 ppm may partially arise from carbons located near sulfoxide-containing environments due to incorporation of DMSO to polymer system. However, the S 2p XPS spectrum showed only a faint signal attributable to oxidized sulfur species, suggesting that such environments, if present, are minor. Beisdes the peaks ^{13}C CP/MAS NMR spectrum is not quantifiable. The peak near 27 ppm is attributed to alkyl carbons in a sulfur- and carbonyl-influenced environment, while the signal at ~ 15 ppm is assigned to methyl carbons. Overall, the spectrum indicates that 2AcPS contains carbonyl groups, conjugated unsaturated carbons, and aliphatic carbons in sulfur-containing environments, consistent with a structurally heterogeneous sulfur–organic polymer network.

UV-Vis analyses

The solid-state UV–Vis diffuse reflectance spectrum of 2AcPS shows distinct optical features in the near-UV and visible regions, with features around approximately 296 nm and 429 nm. (Fig. 7). The feature at ~296 nm may be associated with π–π* transitions of unsaturated carbon domains and/or n–π* transitions of carbonyl-containing structures. The broad visible-region feature around ~429 nm is more consistent with heterogeneous sulfur–organic chromophores or condensation-derived unsaturated structures. This observation is consistent with the solid-state NMR results,

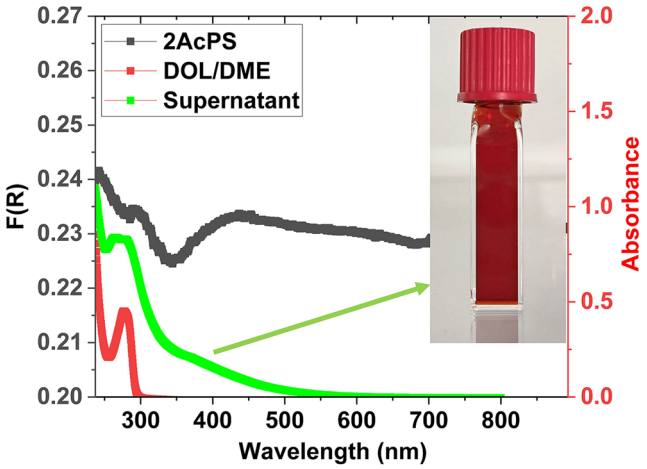


Fig. 7 UV–Vis reflectance spectrum of the pristine 2AcPS sample (measured before soaking) and UV–Vis absorbance spectrum of the DOL/DME-soluble fraction, indicating partial release of soluble oligomeric species. Inset: photograph of the supernatant

which indicate conjugated carbon environments in 2AcPS. After soaking 2AcPS in DOL/DME, the supernatant exhibits strong UV absorption and a broad tail extending into the visible region, while the DOL/DME blank shows no comparable visible absorption. This confirms that DOL/DME extracts soluble chromophoric sulfur–organic species from 2AcPS. This confirms that DOL/DME extracts soluble chromophoric sulfur–organic species from 2AcPS. The mass of the polymer was also measured before and after DOL/DME soaking (approximately 7–8 wt%.). Isothermal TGA analysis, performed by heating to 365 °C and holding at this temperature to estimate the labile/electroactive sulfur fraction, showed that the sulfur-related mass loss decreased only slightly from 45.0 wt% (Fig. 3c) before soaking to ~42.5 wt% after soaking (Fig. S2). If DOL/DME had removed only carbon- and oxygen-containing organic fragments, the sulfur fraction of the remaining solid would be expected to increase. Instead, the observed decrease indicates that sulfur-containing species were also extracted. Therefore, the red supernatant and its UV–Vis absorption are attributed to soluble sulfur–organic chromophoric fragments rather than sulfur-free organic impurities.

Electrochemical testings

2AcPS was selected due to its high polymerized sulfur content for electrochemical testings. Additional characterization of the 2AcPS cathode, including morphology, elemental composition, and crystallinity, is presented in Fig. S3. Carbon nanotubes (MWCNTs) are well-known for their ability to physically confine polysulfides and have even been employed to trap ether-dissolvable electroactive materials [63–65]. As such, we prepared composite cathodes incorporating MWCNTs. Using a MWCNT network alone as the sulfur host may be appealing to mitigate polysulfide shuttle, but the low density of MWCNT networks minimizes the energy density of the cathode [21]. The high surface area of MWCNT networks requires high quantity of electrolyte to impart wettability again decreasing overall gravimetric capacity [21]. Considering that information, we kept the MWCNTs content low. Given 2AcPS is soluble in the electrolyte, one hope is that MWCNTs can partially trap the dissolved polymer species. We set the MWCNT content at 5wt% of the cathode. Additionally, a simple separator conductive carbon (Super P) coating strategy was applied to further enhance trapping of soluble species on the cathode-side of the cell. The electrochemical behavior of the 2AcPS-based cathodes was investigated via cyclic voltammetry (CV), as shown in Fig. 8a and b. The reduction peak at 2.28 V is indication of formation of higher order polysulfides. The second peak at 2.0 V is related to polysulfide transformation into Li_2S_2 or Li_2S [12]. A broad anodic peak associated with the oxidation of these lower-order sulfides back to elemental sulfur (S_8) was also observed. The appearance of two well-defined cathodic peaks suggests that the sulfur chains in 2AcPS contain more than two sulfur atoms. In comparison, disulfide-containing polymers typically exhibit

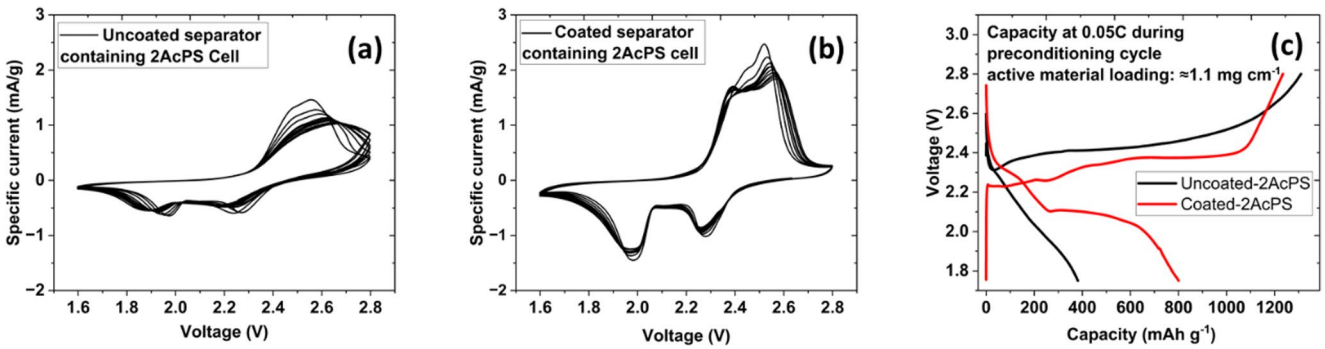


Fig. 8 (**a**–**b**) Cyclic voltammetry (CV) profiles of 2AcPS cells with uncoated and carbon-coated separators, respectively. (**c**) Charge-discharge curves of the same cells during the initial preconditioning cycle at 0.05 C. Capacity and specific current values are normalized to the polymerized/electroactive sulfur fraction of the active material determined by isothermal TGA

only a single cathodic peak and do not support polysulfide formation, which limits their theoretical capacity [66]. Notably, CV curves of the separator-coated cell (SC-2AcPS) exhibit significantly higher current response compared to the uncoated counterpart, suggesting enhanced reaction kinetics and better electrochemical activity. Additionally, a comparison of peak potentials reveals that the polymer cathode with the uncoated separator displays greater polarization: the first and second cathodic peaks appear at 2.26 V and 1.87 V, respectively, whereas these peaks shift to 2.27 V and 1.97 V in the SC-2AcPS cell. This reduction in overpotential in the coated cell is indicative of improved reaction kinetics and reduced internal resistance [67]. The coating adsorbs soluble lithium polysulfides and retains them in close proximity to the cathode, maintaining a higher local concentration of electroactive species and thereby reducing diffusion-limited kinetics. In addition, the conductive nature of the coating improves electronic percolation at the cathode–separator interface, facilitating faster electron transfer during redox reactions. Together with partial suppression of polysulfide shuttle, these effects lead to higher current response and improved overlap of CV curves in successive scans, indicating enhanced reaction kinetics and electrochemical reversibility.

The discharge voltage profiles at 0.05 C for both configurations are presented in Fig. 8c. In conventional Li–S battery, the discharge curve is typically composed of two regions/plateaus. The first plateau is roughly accounts for 25–30% of the discharge capacity [68, 69]. Higher order polysulfides begin to be reduced to short-chain polysulfides (Li_2S_2 and Li_2S) at the potential range around 2.0 V [11]. This step accounts for 75% of capacty. Shuttling is typically manifested as a shortened or suppressed second discharge plateau. In addition, prolonged initial charging can also be attributed to the shuttle effect [1]. If the lithium anode surface is covered with short-chain polysulfides or other reactive species, these can migrate back to the cathode and undergo re-oxidation, resulting in an extended charging period [70]. For instance, Fu et al. reported that cells using diphenyl organotrisulfide as a catholyte displayed an extended first discharge plateau but a highly diminished second plateau, indicative of poor polysulfide retention [66]. A similar phenomenon is observed in the 2AcPS cathode cells examined here. The uncoated separator configuration shows an abnormally elongated first plateau and a truncated second plateau, reinforcing the presence of severe soluble species migration. This supports the interpretation that electroactive material is lost prior to full utilization and highlights the effectiveness of the separator coating strategy in mitigating this issue. Based on these findings, the coated separator was adopted for all further electrochemical characterization to ensure reliable evaluation of the 2AcPS cathode performance.

Cycle stability and rate capability testings

Figure 9a shows the charge and discharge curves at various C-rates of the separator-coated 2AcPS cell. At higher C-rates (≥0.5 C), the voltage plateaus become increasingly sloped and less distinct, indicating increased polarization and kinetic limitations in the sulfur redox reactions. Figure 9b shows the rate capability retention of the cells including both discharge and charge capacities, as the current rate was varied from 0.1 C to 2 C and then returned to 0.1 C. After the preconditioning cycle, at an initial rate of 0.1 C, the cell delivers a high specific capacity of ~850 mAh g^{-1} based on active sulfur content, indicating good sulfur utilization even though sulfur species shuttle during cell operation due to high solubility of 2AcPS in electrolyte. Upon increasing the current rate to 0.2 C, 0.5 C, 1 C, and finally 2 C, the capacity gradually decreases, reflecting the increasing polarization and limited kinetics of redox reactions at higher current densities. Notably, the cell maintains a capacity of ~600 mA h g^{-1} at 0.2 C and ~400 mAh g^{-1} at 0.5 C, while retaining ~200 mA h g^{-1} even at 2 C. However, the observed discrepancy between charge and discharge

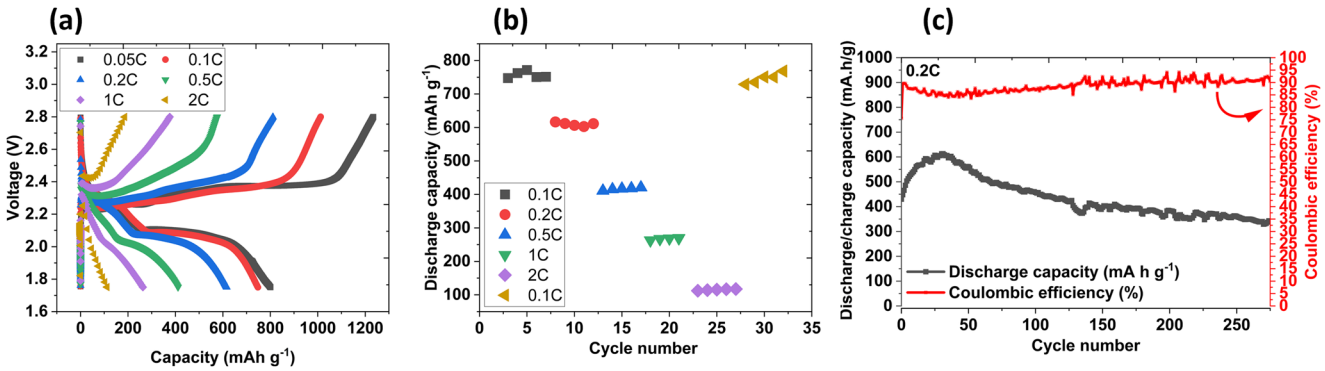


Fig. 9 (**a**, **b**) Rate performance of the 2AcPS cell with a carbon-coated separator from 0.05 C to 2 C and (**c**) cycling stability at 0.2 C. Capacity values are normalized to the polymerized/electroactive sulfur fraction of the active material, as determined by isothermal TGA

capacities indicates a persistently low coulombic efficiency, the origin of which will be discussed in a later section.

Figure 9c presents the long-term cycling performance of the separator-coated 2AcPS cell at 0.2 C over 275 cycles, including discharge capacity and Coulombic efficiency. The 0.2 C rate was selected to approximate moderate operating conditions relevant to applications such as grid-scale energy storage, where discharge rates are typically low [71]. The cell delivers an initial sulfur-specific discharge capacity of ~ 430 mAh g^{-1}, which gradually increases to ~ 615 mAh g^{-1} within the first 30 cycles, likely due to electrode activation and improved contact between cell components [72]. Similar activation behavior has also been reported in other Li–S systems [73]. Beyond 30 cycles, the capacity gradually decreases, reaching ~ 331 mAh g^{-1} after 275 cycles. Thus, approximately 53% of the experimentally observed maximum capacity is retained after 275 cycles. When normalized to the total 2AcPS active-material mass rather than only the electroactive sulfur mass, the maximum experimentally observed capacity corresponds to ~ 277 mAh g^{-1}_{2AcPS}, decreasing to ~ 149 mAh g^{-1}_{2AcPS} after prolonged cycling. The theoretical capacity of 2AcPS, calculated from the electroactive sulfur fraction determined by isothermal TGA, is ~ 753.8 mAh g^{-1}_{2AcPS}. Therefore, the maximum experimentally observed capacity corresponds to approximately 36% of the theoretical 2AcPS capacity, while ~ 20% is retained after long-term cycling.

In terms of Coulombic efficiency, the charge capacity consistently exceeds the discharge capacity, with values initially around 90% that gradually stabilize in the range of 88–92%. Importantly, such coulombic efficiency values would lead to rapid capacity decay if the inefficiency were dominated by irreversible loss mechanisms. The relatively gradual capacity fade observed here instead suggests that a significant fraction of the inefficiency arises from reversible or self-limiting side reactions.

The results are comparable to the studies of Preefer et al. They used a disulfide material and observed a capacity of 150 m Ah g^{-1} in a larger potential window (1.0 V to 3.2 V) [73]. However, they reached almost 100% culombic efficiency. Shadike et al. also produced an organosulfur material with multistep approach and cycled their cathodes between 1.4 and 3.5 V to exploit the activity of carbonyl groups. They obtained around 220 mAh g^{-1} at 0.5 C and after 100 cycles the capacity is around 180 mAh g^{-1} [28], comparable to findings in our study. We note they used a wider potential window, which generally increases the apparent capacity. A comparison of representative organosulfur cathode materials together with their electrochemical performance metrics is summarized in Table S1.

The impedance spectrum of the cell is composed of two semicircles and one tail (Fig. S4). In the equivalent circuit, constant phase element (CPE) is parallel to the impedance elements. CPE is due to non-ideal behavior such as inhomogeneities in electrode material [3]. R_1 could be attributed to many things such as the resistance of the electrolyte, contact resistance or resistance of the active material [70, 74]. This is the intercept of the X-axis of the spectra at the high frequency region. R_2 is the charge transfer resistance and observed in the middle frequency region [70]. R_3 is the interface resistance of the passivation film or solid electrolyte interface. The depressed semicircles such as the one in the middle frequency region may be composed of superpositioned semicircles even though good fitting result is present. As is common, so it is not easy to fully interpret the behavior of cells from impedance spectra.

GITT- impedance spectroscopy and shuttle current measurements

Even with use of a separator coating intended to suppress polysulfide shuttle and improve CE, no significant improvement in CE was observed. This suggests that polysulfide shuttle alone does not account for the charge imbalance and capacity fade in these cells. The persistence of low coulombic efficiency may point to additional degradation/side reaction mechanisms. To elucidate this, we conducted shuttle current measurement (Fig. 10a). During constant voltage holds in Li–S cells equipped with separator coatings, the behavior of the measured current provides critical insight into the underlying electrochemical and chemical processes [68]. In an ideal scenario, where only shuttle-related redox reactions occur, the current initially exhibits a transient negative response. This is followed by a transition to a positive current, which stabilizes once the shuttle flux reaches equilibrium. At this point, the steady-state positive current reflects the rate of oxidation of soluble polysulfide species required to maintain their concentration at the cathode under the applied hold potential. However, in separator-coated 2AcPS cell, the observed positive current deviates. There is no stabilization step, the current continues to increase over time indicating additional processes beyond polysulfide shuttling.

Based on these observations, we infer that the persistently low coulombic efficiency is likely related, at least in part, to the shuttling of electroactive polymer-derived fragments to the lithium anode. These species may undergo irreversible redox reactions and either disrupt the stability of the solid electrolyte interphase (SEI) or contribute to the formation of electronically insulating interfacial layers on the anode. The appearance of additional resistive elements is consistent with such interfacial film formation, as previously reported [72]. The presence of any kind of shuttle can lead to increased interfacial resistance due to the deposition,

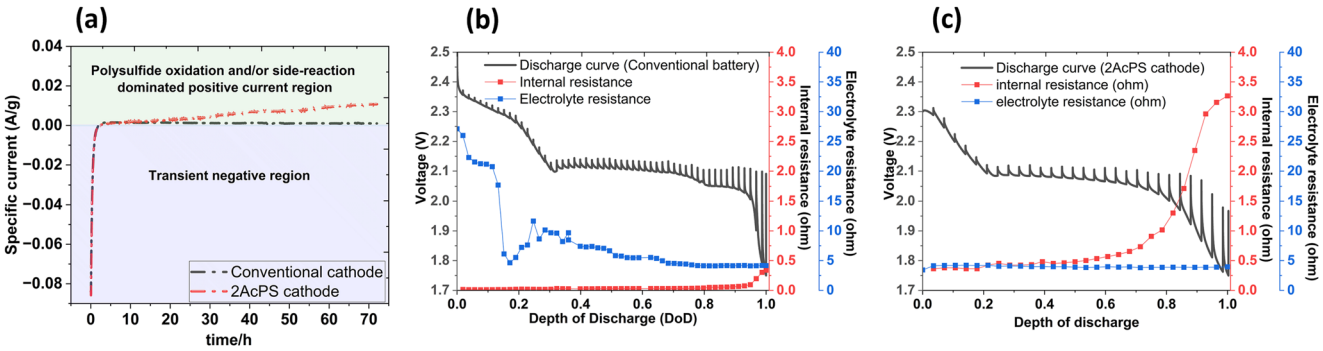


Fig. 10 (**a**) Shuttle current profiles for conventional sulfur cathode and 2AcPS-based polymer cathode. (**b-c**) GITT and impedance-derived internal and electrolyte resistance profiles for a conventional sulfur cathode during discharge

particularly on the lithium anode surface, rendering it progressively more insulating. To investigate this phenomenon, galvanostatic intermittent titration technique (GITT) and electrochemical impedance spectroscopy (EIS) were performed on 2AcPS cell and conventional sulfur cell as shown in Fig. 10b-c (both have conductive carbon separator coating). Notably, impedance measurements were conducted at each GITT step, enabling simultaneous assessment of electrolyte resistance throughout the discharge process.

In conventional battery, internal resistance remains low and stable up until deep discharge due to formation/deposition of Li_2S. In The case of 2AcPS internal resistance increases significantly after 70% discharge. The steep increase in internal resistance corroborates the possibility of formation of resistive polymer fragment layer on anode surface.

In the case of the conventional sulfur battery, the electrolyte resistance decreases until approximately 20% depth of discharge (DoD), which can be attributed to the increased ionic conductivity resulting from the dissolution of sulfur and formation of higher-order polysulfides during the initial discharge plateau. After this point, the electrolyte resistance stabilizes, indicating that the electrolyte composition becomes relatively steady beyond 20% DoD. In contrast, the 2AcPS-based cell exhibits a nearly flat electrolyte resistance throughout the entire discharge process, suggesting that the electrolyte maintains its ionic conductivity and is not significantly altered by precipitation or electrolyte degradation. This further implies that the species responsible for the positive shuttle current observed in the 2AcPS system are not ionic in nature, but rather neutral (e.g., soluble polymer fragments) that can migrate across the separator without contributing to ionic resistance.

To further evaluate the role of soluble polymer-derived species, DOL/DME-soaked/centrifuged 2AcPS was also used as the cathode material. The cathodes were prepared under conditions identical to those used for pristine 2AcPS. However, the DOL/DME-soaked 2AcPS displayed significantly different film-forming behavior. Upon drying, the electrode coating showed a higher tendency to crack, indicating that removal of the soluble fraction alters the mechanical integrity and slurry-processing behavior of the polymer. Moreover, at the same doctor-blade thickness, the DOL/DME-soaked 2AcPS cathode exhibited an areal loading of 1.46 mg cm^{-2}, whereas the pristine 2AcPS cathode showed an areal loading of approximately 1.0–1.3 mg cm^{-2}. This difference suggests that DOL/DME extraction modifies the packing density, drying shrinkage, and/or rheological behavior of the active material. Therefore, the electrochemical behavior of the soaked 2AcPS cathode should be interpreted by considering both the chemical removal of soluble sulfur–organic fragments and the resulting changes in electrode morphology.

Figure 11a, b show the charge–discharge profile and CV curves of the DOL/DME-soaked/centrifuged 2AcPS cathode, respectively. The soaked cathode showed a lower preconditioning capacity than pristine 2AcPS. This lower capacity can be partly attributed to the poorer electrode morphology, including cracking, altered packing, and higher areal loading, which may reduce active-material utilization. Nevertheless, a capacity of approximately 400 mAh g^{-1} was still achieved despite the inhomogeneous cathode film, indicating that the remaining insoluble fraction retained electrochemical activity. This was further confirmed by CV analysis. The cathodic peaks centered around 2.3 V and ~2.0 V, together with the anodic peak around 2.4–2.5 V, are consistent with sulfur-based conversion reactions. More importantly, the pronounced charge/discharge imbalance observed for pristine 2AcPS was largely suppressed after DOL/DME extraction, and the Coulombic efficiency approached unity and slightly exceeded 100%, reaching approximately 104%.

Overall, the improved Coulombic efficiency after DOL/DME extraction indicates that the soluble fraction is not electrochemically innocent. Instead, the soaked 2AcPS cathode shows lower capacity but substantially improved Coulombic efficiency, suggesting that the DOL/DME-soluble fraction is chemically/electrochemically distinct from

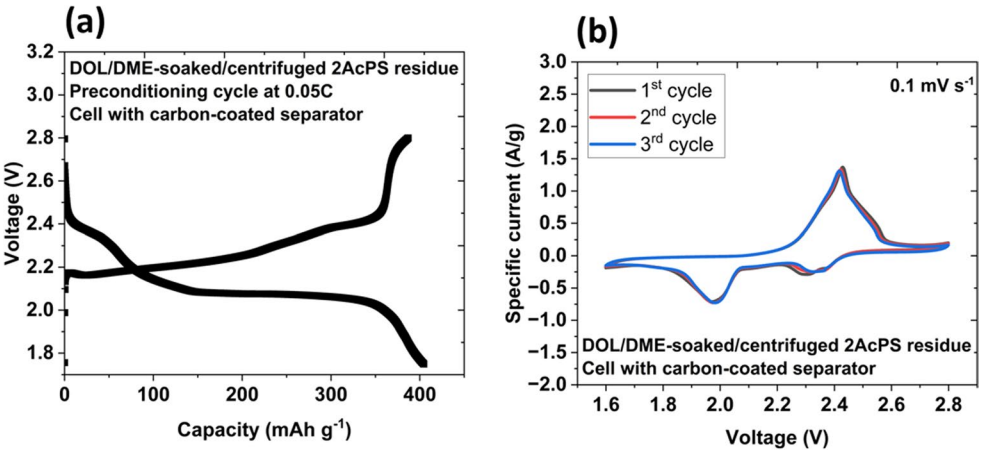


Fig. 11 (**a**) charge–discharge profile and (**b**) CV curves of the DOL/DME-soaked/centrifuged 2AcPS cathode. Capacity and specific current values are normalized to the polymerized/electroactive sulfur fraction of the active material determined by isothermal TGA

the remaining polymer matrix. These soluble species likely retain redox activity and participate in shuttle-related parasitic reactions at the lithium anode.

Discussion

The synthesis of elemental sulfur–containing AcPS samples is influenced not only by the reaction composition but also by the reaction container. Since the reaction runs for ~24 h, if the container is not properly sealed, volatile acetone can easily escape, altering the reaction pathway. We observed that attempts with different vial types produced inconsistent results, highlighting the need for tight sealing and controlled conditions to ensure reproducibility. It is suggested that an acetone-to-sulfur ratio of 2.5:1 provides more reliable polymerization compared to a 2:1 ratio.

In addition, it is well known that excessive dilution during dispersion polymerization—corresponding to a high solvent-to-monomer molar ratio—can lead to the formation of low-molecular-weight polymers [75]. Although the DMSO/S molar ratio employed in this study is sufficient to yield polymeric products, DMSO can be in excess.

Using the slurry casting method, it was not possible to produce cathodes with high areal loading. It is well known that high-capacity retention can be achieved with low active material loading [72]; however, this is not realistic for practical applications. In our case, we employed ~ 1 mg_{sulfur} cm^{-2} active material loading (electroactive sulfur), since at around 1.8 mg_{sulfur} cm^{-2} the electrodes tended to crack and lose mechanical integrity, which limited further loading. This highlights the need for alternative fabrication strategies to achieve higher areal loadings.

While the incorporation of carbonyl functionalities is intended to improve Li^+ mobility and anchor polysulfides through dipolar interactions, these effects may be diminished due to concurrent side reactions that consume active species or destabilize the interface, leading to reduced coulombic efficiency.

Many organosulfur polymers (and sulfur-rich oligomers) can partially dissolve or leach into ether-based electrolytes. Such leached species may (i) decrease the further dissolution of cathode-generated polysulfides by increasing the concentration of sulfur-containing solutes in the electrolyte, and/or (ii) act as a sacrificial/conditioning component that preferentially reacts on Li metal to form a protective interphase—analogous to organo-polysulfide polymers intentionally incorporated into PVDF-based gel polymer electrolytes [76]. However, in the present 2AcPS system, the electrochemical evidence suggests that the soluble polymer-derived fraction is not fully beneficial. GITT/EIS analysis revealed a steep increase in internal resistance during discharge, supporting the formation of a resistive interfacial layer, likely arising from the migration and reaction of polymer-derived fragments at the lithium anode. In addition, DOL/DME extraction removed part of these electroactive soluble polymer-derived fragments from 2AcPS. After their removal, the accessible capacity decreased, but the charge/discharge imbalance was strongly suppressed and the Coulombic efficiency approached unity. This indicates that the soluble polymer-derived species contribute to capacity, but also promote shuttle-related parasitic reactions and interfacial resistance growth. Overall, the value of the present material lies not in immediate performance superiority over optimized sulfur cathodes, but in establishing a new polymer-bound sulfur environment and a new chemistry platform for future Li–S cathode design.

Conclusion

In this work, we report a simple solvent-assisted route for the copolymerization of acetone and sulfur using DMSO as an activating solvent. The reaction yields acetone polysulfide (AcPS), a sulfur-rich organosulfur polymer that forms a cross-linked carbonyl–sulfur network with up to ~59 wt% polymerized sulfur. Structural analyses, including XRD, Raman, FTIR, XPS, solid-state NMR, TG-FTIR, and SEM, confirm

the formation of an amorphous carbonyl–sulfur framework without detectable crystalline sulfur domains. Electrochemical evaluation demonstrates that AcPS is electroactive and can function as a Li–S cathode material. With conductive carbon-coated separators, AcPS cathodes deliver a maximum discharge capacity of ~615 mAh g^{-1}, based on only sulfur mass, at 0.2 C and retain ~331 mAh g^{-1} after 275 cycles, corresponding to ~53% capacity retention. The Coulombic efficiency stabilizes in the range of 88–92%, indicating the presence of ongoing but largely self-limiting and partially reversible side processes rather than continuous irreversible degradation. Shuttle-current measurements combined with GITT/EIS analysis suggest that, in addition to conventional polysulfide shuttling, transient migration and interfacial accumulation of polymer-derived species contribute to efficiency losses without causing rapid cell failure. DOL/DME washing removed part of these soluble polymer-derived fractions, leading to Coulombic efficiencies approaching unity and supporting their role in shuttle-related parasitic reactions. Overall, this study establishes AcPS as a low-cost, solvent-derived sulfur–carbonyl polymer platform for Li–S cathode materials, while also highlighting the need for further optimization to address remaining challenges related to efficiency and long-term interfacial stability. Therefore, the significance of the present material lies not in immediate performance superiority over optimized sulfur cathodes, but in demonstrating a new polymer-bound sulfur environment and a tunable sulfur–organic chemistry platform for future Li–S cathode design.

Supplementary Information The online version contains supplementary material available at https://doi.org/10.1007/s11581-026-07184-w.

Acknowledgements This work was supported by Yildiz Technical University (YTU) under the Research Universities Support Program (ADEP) (Project No. FBA-2024-6061). The authors gratefully acknowledge Prof. Paul V. Braun for valuable scientific discussions and insightful comments on this work. The authors also thank Gerhard Althoff-Ospelt for support with the solid-state NMR analysis and Dr. Çağdaş Dağ for valuable assistance.

Author contributions Conceptualization: Ali Can Zaman; Methodology: Ali Can Zaman; Investigation: Ali Can Zaman; Formal analysis: Ali Can Zaman; Writing – original draft: Ali Can Zaman; Writing – review & editing: Ali Can Zaman, Figen Kaya, Cengiz Kaya; Supervision: Figen Kaya, Cengiz Kaya; Funding acquisition: Ali Can Zaman.

Data availability The data that support the findings of this study are available from the corresponding author upon reasonable request.

Declarations

Competing interests A.C.Z. is an inventor on a Turkish patent application related to this work (Application No. 2024/008568). The other authors declare no competing interests.

References

1. Baek M, Shin H, Char K, Choi JW (2020) New high donor electrolyte for lithium–sulfur batteries. Adv Mater 32(52):2005022. https://doi.org/10.1002/adma.202005022
2. Wu J, Wu Y, Wang L, Ye H, Lu J, Li Y (2024) Challenges and advances in rechargeable batteries for extreme-condition applications. Adv Mater 36(4):2308193. https://doi.org/10.1002/adma.202308193
3. Gröbmeyer A, Becking J, Bieker PM, Winter M, Stan MC (2019) A facile preparation of S_8/C composite cathode for lithium-sulfur cells: influence of intrinsic and extrinsic cathode properties on the electrochemical performance. Energy Technol 7(4):1800789. https://doi.org/10.1002/ente.201800789
4. Canas NA, Hirose K, Pascucci B, Wagner N, Friedrich KA, Hiesgen R (2013) Investigations of lithium-sulfur batteries using electrochemical impedance spectroscopy. Electrochim Acta 97:42–51. https://doi.org/10.1016/j.electacta.2013.02.101
5. Kaiser MR, Chou S, Liu HK, Dou SX, Wang C, Wang J (2017) Structure–Property Relationships of Organic Electrolytes and Their Effects on Li/S Battery Performance. Adv Mater 29:1–17. https://doi.org/10.1002/adma.201700449
6. Li G, Wang X, Seo MH, Li M, Ma L, Yuan Y, Wu T, Yu A, Wang S, Lu J, Chen Z (2018) Chemisorption of polysulfides through redox reactions with organic molecules for lithium–sulfur batteries. Nat Commun 9:705. https://doi.org/10.1038/s41467-018-03116-z
7. Ma L, Zhuang HL, Wei S, Hendrickson KE, Kim MS, Cohn G, Hennig RG, Archer LA (2016) Enhanced Li-S batteries using amine-functionalized carbon nanotubes in the cathode. ACS Nano 10:1050–1059. https://doi.org/10.1021/acsnano.5b06373
8. Ji X, Lee KT, Nazar LF (2009) A highly ordered nanostructured carbon-sulphur cathode for lithium-sulphur batteries. Nat Mater 8:500–506. https://doi.org/10.1038/nmat2460
9. Geng X, Liao Y, Rao M, Li X, Li W (2015) Mesoporous carbon-sulfur composite as cathode for lithium-sulfur battery. Ionics (Kiel) 21:645–650. https://doi.org/10.1007/s11581-014-1227-8
10. Hippauf F, Nickel W, Hao GP, Schwedtmann K, Giebeler L, Oswald S, Borchardt L, Doerfler S, Weigand JJ, Kaskel S (2016) The Importance of Pore Size and Surface Polarity for Polysulfide Adsorption in Lithium Sulfur Batteries. Adv Mater Interfaces 3:1–9. https://doi.org/10.1002/admi.201600508
11. Grace JP, Martha SK (2025) Sulfur-doped biocarbon as a sulfur host and a polysulfide trapping agent in lithium-sulfur batteries. Ionics (Kiel). https://doi.org/10.1007/s11581-025-06308-y
12. Hart CJ, Cuisinier M, Liang X, Kundu D, Garsuch A, Nazar LF (2015) Rational design of sulphur host materials for Li-S batteries: Correlating lithium polysulphide adsorptivity and self-discharge capacity loss. Chem Commun 51:2308–2311. https://doi.org/10.1039/c4cc08980d
13. Huang X, Wang Z, Knibbe R, Luo B, Ahad SA, Sun D, Wang L (2019) Cyclic voltammetry in lithium–sulfur batteries—challenges and opportunities. Energy Technol 7(8):1801001. https://doi.org/10.1002/ente.201801001
14. Liang X, Hart C, Pang Q, Garsuch A, Weiss T, Nazar LF (2015) A highly efficient polysulfide mediator for lithium-sulfur batteries. Nat Commun 6:1–8. https://doi.org/10.1038/ncomms6682
15. Lin YC, Wu YH, Ting JM, Chung SH (2023) Stable Lithium-Sulfur Cell Separator with a High-Entropy Metal Oxide Modification. Energy Fuels 37:15162–15169. https://doi.org/10.1021/acs.energyfuels.3c02538
16. Xiong Z, Zhang G, Ding Y, You J, Cheng S (2023) Thin-walled hollow MoS2 microspheres as sulfur hosts for high-performance lithium sulfur batteries. Int J Electrochem Sci 18:100215. https://doi.org/10.1016/j.ijoes.2023.100215

17. Pang Q, Kwok CY, Kundu D, Liang X, Nazar LF (2019) Lightweight Metallic MgB2 Mediates Polysulfide Redox and Promises High-Energy-Density Lithium-Sulfur Batteries. Joule 3:136–148. https://doi.org/10.1016/j.joule.2018.09.024
18. Li W, Zheng G, Yang Y, W Seh Z, Liu N, Cui Y (2013) High-performance hollow sulfur nanostructured battery cathode through a scalable, room temperature, one-step, bottom-up approach. Proc Natl Acad Sci 110:7148–7153. https://doi.org/10.1073/pnas.1220992110
19. Huang L, Cheng J, Li X, Yuan D, Ni W, Qu G, Guan Q, Zhang Y, Wang B (2015) Sulfur quantum dots wrapped by conductive polymer shell with internal void spaces for high-performance lithium-sulfur batteries. J Mater Chem Mater 3:4049–4057. https://doi.org/10.1039/c4ta06609j
20. Zeng F, Jin Z, Yuan K, Liu S, Cheng X, Wang A, Wang W, Yang YS (2016) High performance lithium-sulfur batteries with a permselective sulfonated acetylene black modified separator. J Mater Chem Mater 4:12319–12327. https://doi.org/10.1039/c6ta02680j
21. Yao H, Yan K, Li W, Zheng G, Kong D, Seh ZW, Narasimhan VK, Liang Z, Cui Y (2014) Improved lithium-sulfur batteries with a conductive coating on the separator to prevent the accumulation of inactive S-related species at the cathode-separator interface. Energy Environ Sci 7:3381–3390. https://doi.org/10.1039/c4ee01377h
22. Bhargav A, He J, Gupta A, Manthiram A (2020) Lithium-Sulfur Batteries: Attaining the Critical Metrics. Joule 4:285–291. https://doi.org/10.1016/j.joule.2020.01.001
23. Ye H, Sun J, Zhao Y, Lee JY (2022) An integrated approach to improve the performance of lean–electrolyte lithium–sulfur batteries. J Energy Chem 67:585–592. https://doi.org/10.1016/j.jechem.2021.11.004
24. Sang P, Chen Q, Wang DY, Guo W, Fu Y (2023) Organosulfur Materials for Rechargeable Batteries: Structure, Mechanism, and Application. Chem Rev 123:1262–1326. https://doi.org/10.1021/acs.chemrev.2c00739
25. Visco SJ, Mailhe CC, De Jonghe LC, Armand MB (1989) A novel class of organosulfur electrodes for energy storage. J Electrochem Soc 136(3):661–664. https://doi.org/10.1149/1.2096706
26. Chen K, Fang R, Lian Z, Zhang X, Tang P, Li B, He K, Wang Dwei, Cheng HM, Sun Z, Li F (2021) An in-situ solidification strategy to block polysulfides in Lithium-Sulfur batteries. Energy Storage Mater 37:224–232. https://doi.org/10.1016/j.ensm.2021.02.012
27. Ye H, Li Y (2023) A perspective on sulfur-equivalent cathode materials for lithium-sulfur batteries. Energy Lab 1(1):220003. https://doi.org/10.54227/elab.20220003
28. Wang DY, Guo W, Fu Y (2019) Organosulfides: An Emerging Class of Cathode Materials for Rechargeable Lithium Batteries. Acc Chem Res 52:2290–2300. https://doi.org/10.1021/acs.accounts.9b00231
29. Shadike Z, Lee HS, Tian C, Sun K, Song L, Hu E, Waluyo I, Hunt A, Ghose S, Hu Y, Zhou J, Wang J, Northrup P, Bak SM, Yang XQ (2019) Synthesis and characterization of a molecularly designed high-performance organodisulfide as cathode material for lithium batteries. Advanced Energy Materials 9:1900705. https://doi.org/10.1002/aenm.201900705
30. Shin H, Kim J, Kim D, Nguyen VH, Lee S, Han S, Lim J, Char K (2018) Aqueous polysulfide-ene polymerization for sulfur-rich nanoparticles and their use in heavy metal ion remediation. J Mater Chem Mater 6:23542–23549. https://doi.org/10.1039/c8ta05457f
31. Song Z, Qian Y, Zhang T, Otani M, Zhou H (2015) Poly(benzoquinonyl sulfide) as a high-energy organic cathode for rechargeable Li and Na batteries. Adv Sci 2(9):1500124. https://doi.org/10.1002/advs.201500124
32. Liu K, Zheng J, Zhong G, Yang Y (2011) Poly(2,5-dihydroxy-1,4-benzoquinonyl sulfide) (PDBS) as a cathode material for lithium ion batteries. J Mater Chem 21:4125–4131. https://doi.org/10.1039/c0jm03127e
33. Bhargav A, Chang CH, Fu Y, Manthiram A (2019) Rationally designed high-sulfur-content polymeric cathode material for lithium-sulfur batteries. ACS Appl Mater Interfaces 11:6136–6142. https://doi.org/10.1021/acsami.8b21395
34. Gomez I, Leonet O, Alberto Blazquez J, Grande HJ, Mecerreyes D (2018) Poly(anthraquinonyl sulfides): High Capacity Redox Polymers for Energy Storage. ACS Macro Lett 7:419–424. https://doi.org/10.1021/acsmacrolett.8b00154
35. Chung WJ, Griebel JJ, Kim ET, Yoon H, Simmonds AG, Ji HJ, Dirlam PT, Glass RS, Wie JJ, Nguyen NA, Guralnick BW, Park J, Somogyi Á, Theato P, Mackay ME, Sung YE, Char K, Pyun J (2013) The use of elemental sulfur as an alternative feedstock for polymeric materials. Nat Chem 5:518–524. https://doi.org/10.1038/nchem.1624
36. Park J, Kim ET, Kim C, Pyun J, Jang HS, Shin J, Choi JW, Char K, Sung YE (2017) The importance of confined sulfur nanodomains and adjoining electron conductive pathways in subreaction Regimes of Li-S batteries. Adv Energy Mater 7:1–10. https://doi.org/10.1002/aenm.201700074
37. Kang H, Kim H, Park MJ (2018) Sulfur-Rich Polymers with Functional Linkers for High-Capacity and Fast-Charging Lithium-Sulfur Batteries. Adv Energy Mater 8:1802423. https://doi.org/10.1002/aenm.201802423
38. Zhang Y, Pavlopoulos NG, Kleine TS, Karayilan M, Glass RS, Char K, Pyun J (2019) Nucleophilic Activation of Elemental Sulfur for Inverse Vulcanization and Dynamic Covalent Polymerizations. J Polym Sci Polym Chem 57:7–12. https://doi.org/10.1002/pola.29266
39. Dodd LJ, Omar Ö, Wu X, Hasell T (2021) Investigating the Role and Scope of Catalysts in Inverse Vulcanization. ACS Catal 11:4441–4455. https://doi.org/10.1021/acscatal.0c05010
40. Limjuco LA, Nisola GM, Parohinog KJ, Valdehuesa KNG, Lee SP, Kim H, Chung WJ (2019) Water-insoluble hydrophilic polysulfides as microfibrous composites towards highly effective and practical Hg2 + capture. Chem Eng J 378:122216. https://doi.org/10.1016/j.cej.2019.122216
41. Krein EB, Aizenshtat Z (1993) Phase Transfer-Catalyzed Reactions between Polysulfide Anions and α,β-Unsaturated Carbonyl Compounds. J Org Chem 58:6103–6108. https://doi.org/10.1021/jo00074a043
42. Chung SH, Manthiram A (2014) Bifunctional separator with a light-weight carbon-coating for dynamically and statically stable lithium-sulfur batteries. Adv Funct Mater 24:5299–5306. https://doi.org/10.1002/adfm.201400845
43. Zhang SS (2012) Effect of Discharge Cutoff Voltage on Reversibility of Lithium/Sulfur Batteries with LiNO 3 -Contained Electrolyte. J Electrochem Soc 159:A920–A923. https://doi.org/10.1149/2.002207jes
44. Wu X, Smith JA, Petcher S, Zhang B, Parker DJ, Griffin JM, Hasell T (2019) Catalytic inverse vulcanization. Nat Commun 10:1–9. https://doi.org/10.1038/s41467-019-08430-8
45. Lian Q, Li Y, Li K, Cheng J, Zhang J (2017) Insights into the Vulcanization Mechanism through a Simple and Facile Approach to the Sulfur Cleavage Behavior. Macromolecules 50:803–810. https://doi.org/10.1021/acs.macromol.6b02335
46. Hou H, Banks CE, Jing M, Zhang Y, Ji X (2015) Carbon Quantum Dots and Their Derivative 3D Porous Carbon Frameworks for Sodium-Ion Batteries with Ultralong Cycle Life. Adv Mater 27:7861–7866. https://doi.org/10.1002/adma.201503816
47. Zaman AC, Kaya F, Kaya C (2024) Synthesis of acetone polysulfide copolymer. Turkish Patent Application No. 2024/008568.
48. Tonkin SJ, Gibson CT, Campbell JA, Lewis DA, Karton A, Hasell T, Chalker JM (2020) Chemically induced repair, adhesion, and recycling of polymers made by inverse vulcanization. Chem Sci 11:5537–5546. https://doi.org/10.1039/d0sc00855a
49. Zaman AC (2022) Sulfur-acetylacetone based solutions for precipitation of quasi-core–shell microparticles or hybrid structures. J Mol Liq 355:118971. https://doi.org/10.1016/j.molliq.2022.118971

50. Zhang Y, Glass RS, Char K, Pyun J (2019) Recent advances in the polymerization of elemental sulphur, inverse vulcanization and methods to obtain functional Chalcogenide Hybrid Inorganic/Organic Polymers (CHIPs). Polym Chem 10:4078–4105. https://doi.org/10.1039/C9PY00636B
51. Pai R, Singh A, Tang MH, Kalra V (2022) Stabilization of gamma sulfur at room temperature to enable the use of carbonate electrolyte in Li-S batteries. Communications Chemistry 5:17. https://doi.org/10.1038/s42004-022-00626-2
52. Wang H, Zhang B, Dop R, Yan P, Neale AR, Hardwick LJ, Hasell T (2022) Oxygen heteroatom enhanced sulfur-rich polymers synthesized by inverse vulcanization for high-performance lithium-sulfur batteries. J Power Sources 545:231921. https://doi.org/10.1016/j.jpowsour.2022.231921
53. Choudhury S, Akef M, Seifert A, Göbel M, Gruschwitz M, Matsidik R, Tegenkamp C, Sommer M (2024) Hybrid Organosulfur Network/MWCNT Composite Cathodes for Li-S Batteries. ACS Appl Mater Interfaces 16:6301–6314. https://doi.org/10.1021/acsami.3c09316
54. Yang H, Huang J, Song Y, Yao H, Huang W, Xue X, Jiang L, Jiang Q, Jiang B, Zhang G (2023) Anionic Hybrid Copolymerization of Sulfur with Acrylate: Strategy for Synthesis of High-Performance Sulfur-Based Polymers. J Am Chem Soc. https://doi.org/10.1021/jacs.3c04746
55. Chao JY, Yue TJ, Ren BH, Gu GG, Lu XB, Ren WM (2022) Controlled disassembly of elemental sulfur: an approach to the precise synthesis of polydisulfides. Angew Chem Int Ed 61(16):e202115950. https://doi.org/10.1002/anie.202115950
56. Yang Q, Cai Z, Zhou Q, Liu D, Ma Y, Liao L, Bai H (2024) Free-Standing Poly(vinyl benzoquinone)/Reduced Graphene Oxide Composite Films as a Cathode for Lithium-Ion Batteries. ACS Appl Mater Interfaces. https://doi.org/10.1021/acsami.4c09748
57. Sevilla M, Fuertes aB (2009) The production of carbon materials by hydrothermal carbonization of cellulose. Carbon N Y 47:2281–2289. https://doi.org/10.1016/j.carbon.2009.04.026
58. Yagmur E, Gokce Y, Tekin S, Semerci NI, Aktas Z (2020) Characteristics and comparison of activated carbons prepared from oleaster (Elaeagnus angustifolia L.) fruit using KOH and ZnCl2. Fuel 267:117232. https://doi.org/10.1016/j.fuel.2020.117232
59. Wang D, Pan Z, Chen G, Lu Z (2021) Glycerol derived mesopore-enriched hierarchically carbon nanosheets as the cathode for ultrafast zinc ion hybrid supercapacitor applications. Electrochim Acta 379:138170. https://doi.org/10.1016/j.electacta.2021.138170
60. Khodabakhshi S, Taddei M, Rudd JA, McPherson MJ, Niu Y, Palmer RE, Barron AR, Andreoli E (2021) Interplay between oxygen doping and ultra-microporosity improves the CO2/N2 separation performance of carbons derived from aromatic polycarboxylates. Carbon N Y 173:989–1002. https://doi.org/10.1016/j.carbon.2020.11.080
61. Wang X, Wang J, Wang D, Dou S, Ma Z, Wu J, Tao L, Shen A, Ouyang C, Liu Q, Wang S (2014) One-pot synthesis of nitrogen and sulfur co-doped graphene as efficient metal-free electrocatalysts for the oxygen reduction reaction. Chem Commun 50:4839–4842. https://doi.org/10.1039/c4cc00440j
62. Tian W, Zhang H, Sun H, Suvorova A, Saunders M, Tade M, Wang S (2016) Heteroatom (N or N-S)-Doping Induced Layered and Honeycomb Microstructures of Porous Carbons for CO 2 Capture and Energy Applications. Adv Funct Mater 26:8651–8661. https://doi.org/10.1002/adfm.201603937
63. TH, Xiaofeng WU, Douglas P (2021) Sulfur - based polymers. US 2021/0324147 A1. https://patents.google.com/patent/US20210324147A1/en?q= (sulfur+inverse+vulcanization)&oq=sulfur+inverse+vulcanization.
64. Bhargav A, Patil SV, Fu Y (2017) A phenyl disulfide@CNT composite cathode for rechargeable lithium batteries. Sustain Energy Fuels 1:1007–1012. https://doi.org/10.1039/c7se00135e
65. Tian S, Yin Y, Cao Z, Yue H, Yang S (2018) Sulfur grown around carbon nanotubes as a cathode material for Li/S battery. Ionics (Kiel) 24:33–41. https://doi.org/10.1007/s11581-017-2165-z
66. Chiu KC, Bhat AL, Yang CK, Chung SH, Tumilty N, Su YS (2025) Advanced Li–S battery configuration featuring sulfur-coated separator and interwoven rGO/CNT fabric current collector. Small 21(8):2405365. https://doi.org/10.1002/smll.202405365
67. Wu M, Bhargav A, Cui Y, Siegel A, Agarwal M, Ma Y, Fu Y (2016) Highly Reversible Diphenyl Trisulfide Catholyte for Rechargeable Lithium Batteries. ACS Energy Lett 1:1221–1226. https://doi.org/10.1021/acsenergylett.6b00533
68. Fan X, Zhang Y, Li J, Yang K, Liang Z, Chen Y, Zhao C, Zhang Z, Mai K (2018) A general dissolution–recrystallization strategy to achieve sulfur-encapsulated carbon for an advanced lithium–sulfur battery. J Mater Chem Mater 6:11664–11669. https://doi.org/10.1039/C8TA02180E
69. Moy D, Manivannan A, Narayanan SR (2014) Direct Measurement of Polysulfide Shuttle Current: A Window into Understanding the Performance of Lithium-Sulfur Cells. J Electrochem Soc 162:A1–A7. https://doi.org/10.1149/2.0181501jes
70. Mikhaylik YV, Akridge JR (2004) Polysulfide Shuttle Study in the Li/S Battery System. J Electrochem Soc 151:A1969. https://doi.org/10.1149/1.1806394
71. Lu Y, Chen J (2020) Prospects of organic electrode materials for practical lithium batteries. Nat Rev Chem 4:127–142. https://doi.org/10.1038/s41570-020-0160-9
72. Zhou QY, Tan L, Lv TB, Li MC, Zhang JJ, Zhao ZQ, Jin XJ, Liu Z, Hou PP, Zeng Z, Deng S, Dai GP (2023) Nickel Foam Coated by Ni Nanoparticle-Decorated 3D Nanocarbons as a Freestanding Host for High-Performance Lithium–Sulfur Batteries. ACS Appl Mater Interfaces 15:3037–3046. https://doi.org/10.1021/ACSAMI.2C19987
73. Preefer MB, Oschmann B, Hawker CJ, Seshadri R, Wudl F (2017) High Sulfur Content Material with Stable Cycling in Lithium-Sulfur Batteries. Angew Chem Int Ed 56:15118–15122. https://doi.org/10.1002/anie.201708746
74. Liu X, Lu Y, Zeng Q, Chen P, Li Z, Wen X, Wen W, Li Z, Zhang L (2020) Trapping of polysulfides with sulfur-rich poly ionic liquid cathode materials for ultralong-life lithium–sulfur batteries. ChemSusChem 13:715–723. https://doi.org/10.1002/cssc.201903122
75. Dong-Chul SN, Pyun RS, Glass RA, Norwood, Jared J (2016) Griebel, Copolymerization of elemental sulfur to synthesize high sulfur content polymeric materials. US20180208686A1. https://patents.google.com/patent/US20180208686A1/en
76. Shen YQ, Zeng FL, Zhou XY, bang Wang A, Wang Wkun, Yuan NY, Ding JN (2020) A novel permselective organo-polysulfides/PVDF gel polymer electrolyte enables stable lithium anode for lithium–sulfur batteries. J Energy Chem 48:267–276. https://doi.org/10.1016/j.jechem.2020.01.016

Publisher's Note Springer Nature remains neutral with regard to jurisdictional claims in published maps and institutional affiliations.

Springer Nature or its licensor (e.g. a society or other partner) holds exclusive rights to this article under a publishing agreement with the author(s) or other rightsholder(s); author self-archiving of the accepted manuscript version of this article is solely governed by the terms of such publishing agreement and applicable law.